Mon. Not. R. Astron. Soc. **000**, 000–000 (0000) Printed 20 November 2000 (MN LaTeX style file v1.4)

THE DEEP X-RAY RADIO BLAZAR SURVEY (DXRBS) II. New Identifications

Hermine Landt[1,2], Paolo Padovani[1,3,4], Eric S. Perlman[1,5], Paolo Giommi[6], Hayley Bignall[7], Anastasios Tzioumis[8]

[1] *Space Telescope Science Institute, 3700 San Martin Drive, Baltimore, MD 21218, USA*
[2] *Hamburger Sternwarte, Gojenbergsweg 112, D-21029 Hamburg, Germany*
[3] *Affiliated to the Astrophysics Division, Space Science Department, European Space Agency*
[4] *On leave from Dipartimento di Fisica, II Università di Roma "Tor Vergata", Via della Ricerca Scientifica 1, I-00133 Roma, Italy*
[5] *Current Address: Physics Department, UMBC, 1000 Hilltop Circle, Baltimore, MD 21250, USA*
[6] *BeppoSAX Science Data Center, ASI, Via Corcolle 19, I-00131 Roma, Italy*
[7] *Department of Physics and Mathematical Physics, University of Adelaide, SA 5005, Australia*
[8] *Australia Telescope National Facility, CSIRO, P.O. Box 76, Epping, NSW 2121, Australia*

Accepted , Received

ABSTRACT

We have searched the archived, pointed *ROSAT* Position Sensitive Proportional Counter data for blazars by correlating the WGACAT X-ray database with several publicly available radio catalogs, restricting our candidate list to serendipitous X-ray sources with a flat radio spectrum ($\alpha_{\rm r} \leq 0.70$, where $S_\nu \propto \nu^{-\alpha}$). This makes up the Deep X-ray Radio Blazar Survey (DXRBS). Here we present new identifications and spectra for 106 sources, including 86 radio-loud quasars, 11 BL Lacertae objects, and 9 narrow-line radio galaxies. Together with our previously published objects and already known sources, our sample now contains 298 identified objects: 234 radio-loud quasars (181 flat-spectrum quasars: FSRQ [$\alpha_{\rm r} \leq 0.50$] and 53 steep-spectrum quasars: SSRQ), 36 BL Lacs, and 28 narrow-line radio galaxies. Redshift information is available for 96% of these. Thus our selection technique is $\sim 90\%$ efficient at finding radio-loud quasars and BL Lacs. Reaching 5 GHz radio fluxes ~ 50 mJy and $0.1 - 2.0$ keV X-ray fluxes a few $\times 10^{-14}$ erg cm^{-2} s^{-1}, DXRBS is the faintest and largest flat-spectrum radio sample with nearly complete ($\sim 85\%$) identification. We review the properties of the DXRBS blazar sample, including redshift distribution and coverage of the X-ray-radio power plane for quasars and BL Lacs. Additionally, we touch upon the expanded multiwavelength view of blazars provided by DXRBS. By sampling for the first time the faint end of the radio and X-ray luminosity functions, this sample will allow us to investigate the blazar phenomenon and the validity of unified schemes down to relatively low powers.

Key words: BL Lacertae objects: general – Quasars: general – radio continuum – surveys – X-rays

1 INTRODUCTION

Blazars are the most extreme variety of active galactic nuclei (AGN) known. Their signal properties include irregular, rapid variability; high optical polarization; core-dominant radio morphology; flat ($\alpha_{\rm r} \lesssim 0.5$) radio spectra; apparent superluminal motion; and a broad continuum extending from the radio through the gamma-rays. The broadband emission from blazars is dominated by non-thermal processes (synchrotron and inverse-Compton radiation), likely emitted by a relativistic jet pointed close to our line of sight (as originally proposed by Blandford & Rees in 1978). The properties of misdirected blazars are consistent with those of radio galaxies, which form the so-called "parent population" within unified schemes (e.g., Urry & Padovani 1995).

As a consequence of their peculiar orientation with respect to our line of sight, blazars represent a rare class of sources, which make up considerably less than 5% of all AGN (Padovani 1997). Therefore, currently available blazar samples suffer from small number statistics and relatively high limiting fluxes (~ 1 Jy and a few $\times 10^{-13}$ erg cm^{-2} s^{-1} in the radio and X-ray band respectively). The small size of these samples ($\sim 30-50$ objects) implies, for example, that the derivation of the beaming parameters based on luminosity function studies (e.g., Padovani & Urry 1990; Urry, Padovani & Stickel 1991) is considerably uncertain, especially at low powers. Moreover, our understanding of the blazar phenomenon is mostly based on relatively bright and intrinsically luminous sources, which means we have only sampled the tip of the iceberg of the blazar population.

In Paper I (Perlman et al. 1998) we presented the methods, the first 85 identifications, and some preliminary results of the Deep X-ray Radio Blazar Survey (DXRBS), a large-area ($\lesssim 1,900$ deg^2 depending on the X-ray flux) survey, which reaches relatively faint X-ray (a few $\times 10^{-14}$ erg cm^{-2} s^{-1}) and radio (~ 50 mJy, depending on declination) fluxes. The newly identified DXRBS blazars expanded the range of $L_{\rm x}/L_{\rm r}$ values found among blazars with emission lines by an order of magnitude, and for the first time sampled the faint end of the radio luminosity function of flat spectrum radio quasars (FSRQ) and BL Lacs with reasonable statistics. Moreover, a large fraction of DXRBS BL Lacs were of the so-called "intermediate" type, i.e., spanning a range of $L_{\rm x}/L_{\rm r}$ values in between the classical low-energy peaked BL Lacs (LBL) and high-energy peaked BL Lacs (HBL; Padovani & Giommi 1995). This region of parameter space was almost completely unexplored until very recently (but see also Laurent-Muehleisen et al. 1998).

This paper presents new identifications for 106 sources. In Section 2 we briefly describe the DXRBS sample and the selection technique and discuss the radio spectral indices we obtained in the context of source selection. Section 3 discusses the results of our optical spectroscopy and the makeup of the DXRBS blazar sample as of July 2000. Section 4 reviews some of the sample properties, in particular the redshift distribution. Our conclusions are summarized in Section 5.

2 THE DXRBS SAMPLE

The selection technique and identification procedures used for DXRBS have been described in detail in Paper I. In § 2.1 we briefly summarize the main points, while in § 2.2 we discuss the derivation of the radio spectral index, the main criterion for our candidate selection.

2.1 Candidate Selection

DXRBS takes advantage of the fact that all blazars are relatively strong X-ray and radio emitters. Therefore, selecting X-ray and radio sources with flat radio spectrum (one of the defining properties of the blazar class) is a very efficient way of finding these rare sources. By adopting a spectral index cut $\alpha_{\rm r} \leq 0.7$ DXRBS: 1. selects all FSRQ (defined by $\alpha_{\rm r} \leq 0.5$); 2. selects basically all BL Lacs; 3. excludes the large majority of radio galaxies.

DXRBS uses a cross-correlation of all serendipitous X-ray sources in the publicly available *ROSAT* database WGACAT (first revision: White, Giommi & Angelini 1995), having quality flag ≥ 5 (to avoid problematic detections), with a number of publicly available radio catalogs. North of the celestial equator, we used the 20 cm and 6 cm Green Bank survey catalogs NORTH20CM and GB6 (White & Becker 1992; Gregory et al. 1996), while south of the equator we used the 6 cm Parkes-MIT-NRAO catalog PMN (Griffith & Wright 1993). All sources with radio spectral index $\alpha_{\rm r} \leq 0.7$ at a few GHz and off the Galactic plane ($|b| > 10^\circ$) were selected as blazar candidates.

For objects south of the celestial equator, where a survey at a frequency different from the one of the PMN (6 cm) was missing when we started this project (the NVSS [Condon et al. 1998], now available, reaches in any case only $\delta = -40^\circ$), we conducted a snapshot survey with the Australia Telescope Compact Array (ATCA) at 3.6 and 6 cm. This not only gave us arcsecond radio positions for our southern sources (we use the NVSS for the northern ones) but also radio spectral indices unaffected by variability. In § 2.2 we will compare the spectral indices derived from these different surveys.

The details of the cross-correlations and the criteria for the definition of the sample are given in Paper I. Briefly, the *ROSAT* WGACAT was initially correlated with the GB6 and PMN catalogs with a radius of $1'$. The correlation radius was then expanded to $1.5'$ for the inner $30'$ of the *ROSAT* Position Sensitive Proportional Counter (PSPC) field of view, excluding sources for which the ratio between X-ray/radio offset and positional error was larger than 2 (and therefore likely to be spurious). A radius of $1.5'$ is roughly equal to twice the combined X-ray and radio positional uncertainty of a source with PSPC offset $\sim 30'$ and radio flux ~ 50 mJy (the typical radio flux limit of the PMN, which is declination dependent; in the north our flux limit is given by the NORTH20 [> 100 mJy at 20 cm]).

In the meantime, we have somewhat expanded our criteria to increase completeness. First, in the inner $\sim 30'$ of the PSPC field of view we have included flat-spectrum radio sources with ratio of X-ray/radio offset to positional error between 2.0 and 2.5. Second, we have added sources in the $30' - 45'$ PSPC offset range having a correlation radius with the GB6 and PMN catalogs up to $1.5'$.

A preliminary comparison of the radio flux distributions in the inner $(0' - 30')$ and outer $(30' - 45')$ regions of the PSPC shows no dependence on the PSPC offset for $f_{\rm r} \gtrsim 50$ mJy. Therefore we expect to be complete down to this radio flux up to $45'$. A detailed discussion of the completeness of DXRBS will be presented in a future paper.

2.2 The Radio Spectral Index

One of the strengths of DXRBS is the radio spectral index cut which allows us to take advantage of one of the defining blazar properties, a relatively flat radio spectrum, to select blazars very efficiently. Ideally, the selection should be done primarily on radio core-dominance, the ratio between core and extended radio flux, known to be $\gtrsim 1$ in blazars (e.g., Murphy, Browne & Perley 1993; Perlman & Stocke 1993; Kollgaard et al. 1996), but derivation of this parameter requires dedicated radio observations. DXRBS makes use of the fact that the more core-dominated an object is, the flatter its radio spectral index (Impey & Tapia 1990), and sets the cut at $\alpha_{\rm r} = 0.7$ to guarantee inclusion of all BL Lacs. (This is the limiting value for the BL Lacs with X-ray-to-radio flux ratios typical of our survey within the multiwavelength AGN catalog of Padovani, Giommi & Fiore 1997). Additionally, this cut excludes the majority of radio galaxies.

The radio spectral indices for DXRBS sources have been derived as follows:

- $\delta > 0^\circ$: from the GB6 and NORTH20 catalogues; $\alpha_{\rm r}$ therefore covers the $1.4 - 5$ GHz range ($6 - 20$ cm);
- $\delta < -40^\circ$: from our own ATCA snapshot survey; $\alpha_{\rm r}$ therefore covers the $4.8 - 8.6$ GHz range ($3.6 - 6$ cm);
- $-40^\circ < \delta < 0^\circ$: in this declination range we have access to our ATCA observations and also to PMN-NVSS data ($1.4 - 5$ GHz range). For consistency with the northern part of the survey, we decided to use PMN-NVSS data.

In the following we review the ATCA observations and discuss this latter point.

2.2.1 The ATCA Observations

The ATCA survey was undertaken in two parts: 163 sources with $\delta < -15^\circ$ were observed on 1995 November 11-13; and a further 108 sources (four of which were repeat observations because of bad data during the first run) were observed on 1997 October 27-28. During this second run we included all sources south of $\delta = 0^\circ$. We observed at 4.8 and 8.6 GHz since confusion due to nearby sources within the primary beam is more severe at lower frequencies for a snapshot survey like ours.

The ATCA data were reduced using the MIRIAD software package. During the observations, target sources were interleaved with secondary calibrators which were used for phase calibration. The absolute flux density scale was determined from the primary calibrator PKS 1934−638. Over an entire observing run, typically 3 snapshots, each lasting 2 minutes, were taken for every source. These snapshots were separated in hour angle by roughly 4 hours, with some adjustments made to allow the schedule to run smoothly. This procedure allowed efficient observation of a large number of objects. However, as the ATCA is a linear array with only 6 antennae, the coverage of the (u, v) plane obtained for each source was clearly very limited.

The calibrated data were imaged, and source positions were found from a fit to the peak pixel in the image. While these positions are accurate to $\sim 1''$ for compact sources, the very sparse (u, v) coverage resulted in poor quality images. For an extended source with no compact "core," the position of the brightest pixel is dependent on the sampling, hence the positional error for an extended source may be larger than a few arcseconds.

Source flux densities were estimated directly from the calibrated visibilities. A lower limit to the total flux density of each source was estimated from the visibilities corresponding to the shortest baseline (337 m and 153 m for the data taken in 1995 and 1997 respectively). For 1995, when the majority of the ATCA data were collected, this shortest available baseline gives a synthesised beam of FWHM $\sim 50''$ at 4.8 GHz (half of this at 8.6 GHz). Thus, for sources which have extended emission with angular diameter much larger than this, some of the extended emission is missing in this ATCA data.

The longest baseline in the ATCA is close to 6 km, which results in $2''$ resolution at 4.8 GHz and $1''$ resolution at 8.6 GHz. Due to the sparse sampling of the (u, v) plane mentioned above, there are no sufficient data to fit a detailed model to a complex source, or to make a detailed image of a source with extended structure. The level of extended structure in each source was estimated by comparing the visibility amplitudes corresponding to the flux density for the shortest and longest spacings in the dataset and confirmed by visual examination of plots of amplitude versus distance in the (u, v) plane.

To calculate the flux density of the unresolved, compact component, a point source was fitted to the visibilities of each source using the MIRIAD task *uvfit*. There are two contributions to the error in measurement of the flux density of a point source: a random noise component of the order of 1 mJy rms, and a calibration error which is estimated to be no larger than 2% of the total source flux density. Thus the flux density of an unresolved source is measured to high accuracy. However, the amount of possible large-scale structure is inherently uncertain in measurements with a sparse interferometric array such as the ATCA. Hence, the estimated total flux density of each source should be considered as a lower limit only.

2.2.2 Comparison between ATCA and PMN-NVSS spectral indices

Besides allowing us to select candidates for spectroscopy in advance of the completion of the NVSS, the original stated purpose of the ATCA observations (Paper I) was to help us gauging the effect of using non-simultaneous data to derive spectral indices, and hence to include in our sample true blazars which might otherwise be excluded. Our ATCA data give us radio spectral indices unaffected by variability, since the observations at both frequencies are truly simultaneous, but in a higher frequency range than that used for our northern objects. On the other hand, radio spectral indices derived from PMN-NVSS data cover the more standard $1.4 - 5$ GHz and are less affected by either spatial filtering or poor (u, v) coverage, but involve non-simultaneous data and have angular resolution no better than $\sim 15''$ (Condon et al. 1998). The PMN-NVSS radio spectral indices were derived by summing up all NVSS sources within $3'$ from the PMN position, given the different beam sizes of the two surveys. (Padovani et al., in preparation, show that this procedure is robust and gives radio spectral indices in very good agreement with those derived from single

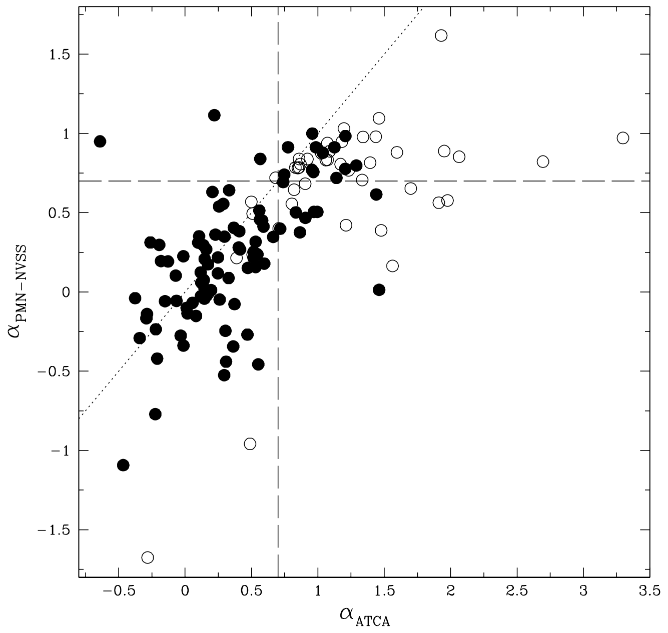

Figure 1. The radio spectral index derived from PMN - NVSS data (1.4 – 5 GHz) compared with the radio spectral index from our ATCA observations (4.8 – 8.6 GHz). The dotted line represents the locus of $\alpha_{\rm PMN-NVSS} = \alpha_{\rm ATCA}$, while the dashed lines indicates $\alpha_{\rm r} = 0.7$ derived in each way. Objects with ATCA core dominance parameter at 4.8 GHz $R_{4.8} > 1$ are plotted as filled circles, while open circles indicate sources with $R_{4.8} < 1$. See text for discussion.

dish measurements.) We expect the values of $\alpha_{\rm ATCA}$ to be correlated with $\alpha_{\rm PMN-NVSS}$, with perhaps a small offset indicative of steepening in the synchrotron spectrum at higher frequencies.

In Figure 1 we compare the values of $\alpha_{\rm ATCA}$ and $\alpha_{\rm PMN-NVSS}$ for all sources in the declination range $-40^\circ < \delta < 0^\circ$. The locus of equal spectral indices is represented by a dotted line. As expected, while the scatter is fairly large, probably due to variability and to the different spatial scales sampled by the PMN/NVSS surveys and the ATCA (see below), the two spectral indices are well correlated ($P > 99.99\%$).

The mean values of the two spectral indices are however somewhat different. We find $\langle\alpha_{\rm ATCA}\rangle = 0.62 \pm 0.06$ while $\langle\alpha_{\rm PMN-NVSS}\rangle = 0.36 \pm 0.04$, and a mean difference of $\langle\Delta\alpha\rangle = \langle\alpha_{\rm ATCA} - \alpha_{\rm PMN-NVSS}\rangle = 0.26 \pm 0.04$. This comparison includes all sources and is therefore not appropriate: an extended source, which will typically have a relatively steep $\alpha_{\rm PMN-NVSS}$, will be resolved out more at 8.6 GHz than at 4.8 GHz with the ATCA, due to the smaller primary beam area at the higher frequency. Such a source will therefore have an even steeper $\alpha_{\rm ATCA}$. A more meaningful comparison is that between the two spectral indices for relatively compact sources, which are the ones we are interested in. For this purpose, we estimated a core-dominance parameter, i.e. the ratio between core and extended flux, from our ATCA data at 4.8 GHz. Note that only a lower limit is available for the extended flux and therefore our core-dominance parameters are upper limits to the true value.

Keeping all this in mind, Figure 1 shows the distribution of the two spectral indices for sources with core-dominance parameter at 4.8 GHz $R_{4.8} > 1$ (filled points) and $R_{4.8} < 1$ (open points). As expected, most of the lobe-dominated ($R_{4.8} < 1$) sources have both $\alpha_{\rm ATCA}$ and $\alpha_{\rm PMN-NVSS} > 0.5 - 0.7$. The difference between the two spectral indices is clearly reduced for core-dominated objects. We find $\langle\alpha_{\rm ATCA}\rangle = 0.36 \pm 0.05$, while $\langle\alpha_{\rm PMN-NVSS}\rangle = 0.23 \pm 0.04$, and a mean difference of $\langle\Delta\alpha\rangle = 0.13 \pm 0.04$.

In the case of a direct proportionality between the two spectral indices, all sources should populate the two areas of the diagram defined by $\alpha_{\rm ATCA} < 0.7$, $\alpha_{\rm PMN-NVSS} < 0.7$ and $\alpha_{\rm ATCA} > 0.7$, $\alpha_{\rm PMN-NVSS} > 0.7$ (the bottom-left and top-right areas, denoted in Figure 1 by the two dashed lines). This is "almost" the case: only 23/138 (17%) of the sources fall outside these regions. By choosing as our selection criterion for inclusion in the sample $\alpha_{\rm PMN-NVSS} < 0.7$, we are conservatively including most (19/23) of these outliers. Ten of these sources, however, have $R_{4.8} < 1$ and their blazar classification might be questionable. As regards the four sources in the top-left part of the figure, excluded by our criterion, one has $R_{4.8} < 1$, while the maps of the other three show that they are at least partially extended.

Some of the sources in Figure 1 with flat $\alpha_{\rm PMN-NVSS}$ but marked ($\gtrsim 0.6$) steepening at high frequencies could be GigaHertz peaked spectrum (GPS) sources (e.g., O'Dea 1998). For these sources, and for those with $\alpha_{\rm ATCA} > 0.7$, we give the $\alpha_{\rm ATCA}$ values as footnotes to Table 5.

Thus our conclusion is that among our sources we observe a steepening in spectral index between 1.4 – 5.0 GHz and 4.8 – 8.6 GHz of $\langle\Delta\alpha\rangle \sim 0.25$, which reduces to 0.13 when considering only the sources likely to be compact. By applying the same cut of $\alpha_{\rm r} = 0.7$ in the declination range $\delta < -40^\circ$, where we have only 4.8 – 8.6 GHz spectral indices available for our candidate selection, we are missing no more than three blazar candidates, included otherwise if $\alpha_{\rm PMN-NVSS}$ were available and less than 0.5 (as the majority of our blazars are FSRQ). We estimate this number by considering the sources included in Fig. 1 with $\alpha_{\rm ATCA} > 0.7$. Of these, only 7% have $\alpha_{\rm PMN-NVSS} < 0.5$ and $R_{4.8} > 1$. Therefore, the use of higher resolution data in a slightly different frequency range does not affect strongly our selection of blazar candidates.

As discussed in § 3.2, spectral indices over a relatively limited frequency range are used to establish the blazar nature of a source. Are all our quasars with $\alpha_{\rm r} \leq 0.5$ blazars? Are they all core-dominated? We plan to address these questions in our future work with the help of our ATCA maps, and dedicated, high resolution radio observations.

3 THE IDENTIFICATIONS

The DXRBS sample now comprises about 350 candidates of which $\sim$ 85% are identified. In Paper I, classifications for 85 newly identified objects and 97 previously known sources were given. In this section we present 102 additional new identifications and 4 higher signal-to-noise ratio (SNR) spectra for objects previously published in Paper I, namely WGAJ0421.5+1433, WGAJ0528.5−5820, WGA J1057.6−7724 and WGAJ1222.6+2934. Note that, as stated in Paper I, the newly identified objects include not only objects meeting the strict selection criteria but also some lower priority sources (DXRBS objects at low Galactic latitude, below the radio completeness limits, or with $\alpha_r > 0.7$). These are marked with an asterisk in Table 5.

3.1 Identifying Candidates for Optical Spectroscopy

Accurate ($\lesssim 3''$) positions to pinpoint the optical counterpart and allow spectroscopical identification were obtained from the NVSS or from our ATCA observations. Finders were produced using the Digitized Sky Survey (DSS) via SkyCat (Albrecht et al. 1997). Magnitudes were derived for relatively bright objects ($B \lesssim 22$, $R \lesssim 20$) from the Cambridge APM project (Irwin, Maddox & McMahon 1994) for the northern sources and Edinburgh COSMOS catalogue for the southern objects (Drinkwater, Barnes & Ellison 1995). Candidates without counterparts on DSS plates were imaged at the KPNO 0.9 m, WIYN 3.5 m, CTIO 0.9 m, and ESO 2.2 and 3.6 m telescopes.

Spectroscopic observations were conducted at the KPNO 2.1 m and 4 m, and at the ESO 2.2 m and 3.6 m telescopes. Multiple grisms were used in some runs in order to maximize SNR for faint objects and obtain higher dispersion for brighter objects. In Table 1 we list the resolution and approximate wavelength range of the grisms used in our telescope runs. In Table 2 we list the details of the observations. Since we expected most of our sources to be quasars, the exposure times were calculated based on this assumption. This rendered the identification of weak emission and absorption features in our spectra rather difficult. The spectra acquired during the September 1998 and February 1999 runs have a fairly low SNR due to bad weather conditions. Spectra observed with the ESO 3.6 m and KPNO 4 m were taken at parallactic angle, except in cases where the radio/X-ray error circle contained two candidates. Observations at parallactic angle were not possible at the ESO 2.2 m and KPNO 2.1 m telescopes, which require a manual slit rotation.

The acquired spectra were reduced using standard IRAF routines. The data were bias-subtracted and flatfielded using programs in the IRAF package *noao.imred.ccdred*, and the spectra were extracted, wavelength and flux-calibrated using programs in the package *noao.twodspec*. Cosmic rays were removed in the 1 and 2-dimensional data by hand. A dereddening correction was applied to the data using the IRAF routine *noao.onedspec.dered* and assuming Galactic values of extinction derived from 21-cm measurements (Stark et al. 1992).

Positional information for all sources for which we announce new or refined identifications herein are given in Table 4, including information from WGACAT and the PMN or GB6 surveys. Column (1) gives the WGA name of the source, columns (2) and (3) give the WGA position, column (4) gives the source offset from the center of the PSPC field of view, in arcmin, columns (5) and (6) give the PMN or GB6 position, columns (7) and (8) give the position of the optical counterpart (which is taken as the position of the corresponding NVSS or ATCA source if within $\sim 3''$; otherwise the optical position was measured on the finder and a footnote is given). Finally, column (9) gives the offset between the WGA (X-ray) and optical position, in arcsec, while column (10) gives the ratio between the latter offset (column 9) and the sum in quadrature of the X-ray and optical (radio) positional error. The value in column (10) corresponds roughly to the significance in σ's of the X-ray/radio mismatch (e.g., a value of 2.0 implies a 95% probability that the X-ray/radio match is random; see Paper I for details). The chance radio/optical identification is very small. Using a $3''$ radio positional uncertainty, the number of previously unidentified sources in DXRBS (~ 250), and a background density of stellar objects and galaxies from faint UK Schmidt plates of 2.1 stars and 1.2 galaxies per arcmin^2 (e.g., Jauncey et al. 1982), one obtains ~ 6 chance coincidences (or $\sim 2\%$).

A number of DXRBS sources were serendipitously observed by *ROSAT* on more than one occasion; for completeness, we give WGACAT positions for all observations. The WGACAT positional error is not stated individually but is a function of the offset from the center of the PSPC, i.e. column (4), and can be derived from this value using Table 3 (see also Paper I).

Table 1. Grism Properties

Telescope	Dispersion (Å/pix)	Range (Å)
KPNO 2.1 m	4.6	4000−10000
KPNO 4 m	9.1	4300−10000
	4.3	4300− 8500
	4.3	4800− 9500
ESO 2.2 m	8.4	3400− 9200
ESO 3.6 m	6.3	3185−10940
	25.0	3600−11000
	6.3	3740− 6950
	2.1	3860− 8070

Table 3. X-ray Positional Errors

PSPC Center Offset	WGACAT Positional Error
$0 - 10'$	$13.0''$
$10 - 20'$	$18.1''$
$20 - 30'$	$28.6''$
$30 - 40'$	$36.1''$
$40 - 50'$	$42.0''$
$50 - 60'$	$53.4''$

Table 2. Log of Observations

Name	Observatory	Date	Exp [sec]	Name	Observatory	Date	Exp [sec]
WGAJ0010.5−3027	ESO 3.6 m	1998 Sep	900	WGAJ1320.4+0140	ESO 3.6 m	1999 Mar	1200
WGAJ0014.5−3059	ESO 3.6 m	1998 Sep	1200	WGAJ1323.8−3653	ESO 3.6 m	1998 Feb	2400
WGAJ0034.4−2133	ESO 3.6 m	1998 Sep	3600	WGAJ1329.0+5009	KPNO 4 m	1999 Feb	1800
WGAJ0106.7−1034	KPNO 2.1 m	1998 Jun	1200	WGAJ1332.7+4722	KPNO 2.1 m	1998 Jun	2400
WGAJ0126.2−0500	ESO 3.6 m	1998 Sep	900	WGAJ1333.1−3323	ESO 3.6 m	1999 Mar	1800
WGAJ0227.5−0847	ESO 3.6 m	1998 Sep	900	WGAJ1337.2−1319	ESO 2.2 m	1997 May	1500
WGAJ0251.9−2051	ESO 3.6 m	1999 Mar	600	WGAJ1353.2−4720	ESO 3.6 m	1999 Mar	1200
WGAJ0305.3−2420	KPNO 4 m	1999 Feb	600	WGAJ1359.6+4010	KPNO 2.1 m	1998 Jun	1200
WGAJ0307.7−4717	ESO 3.6 m	1999 Mar	2700	WGAJ1400.7+0425	ESO 3.6 m	1998 Feb	900
WGAJ0322.1−5205	ESO 3.6 m	1998 Feb	300	WGAJ1402.7−3334	ESO 3.6 m	1998 Feb	1800
WGAJ0322.6−1335	ESO 3.6 m	1998 Feb	2400	WGAJ1404.2+3413	KPNO 4 m	1999 Feb	1200
WGAJ0421.5+1433	ESO 3.6 m	1998 Feb	1200	WGAJ1406.9+3433	KPNO 2.1 m	1998 Jun	1200
WGAJ0427.2−0756	ESO 3.6 m	1998 Feb	1200	WGAJ1416.4+1242	ESO 2.2 m	1997 May	900
WGAJ0438.7−4727	ESO 3.6 m	1999 Mar	2700	WGAJ1417.5+2645	ESO 2.2 m	1997 May	1800
WGAJ0513.8+0156	ESO 3.6 m	1999 Mar	600	WGAJ1419.1+0603	ESO 2.2 m	1997 May	1800
WGAJ0528.5−5820	ESO 3.6 m	1999 Mar	900	WGAJ1420.6+0650	ESO 2.2 m	1997 May	900
WGAJ0533.7−5817	ESO 3.6 m	1999 Mar	900	WGAJ1423.3+4830	KPNO 2.1 m	1998 Jun	2400
WGAJ0534.9−6439	ESO 3.6 m	1999 Mar	900	WGAJ1427.9+3247	KPNO 4 m	1999 Feb	1200
WGAJ0646.8+6807	KPNO 4 m	1999 Feb	2400	WGAJ1442.3+5236	KPNO 2.1 m	1998 Jun	2700
WGAJ0651.9+6955	KPNO 4 m	1999 Feb	1800	WGAJ1457.7−2818	ESO 2.2 m	1997 May	1200
WGAJ0741.7−5304	ESO 3.6 m	1999 Mar	3600	WGAJ1457.9−2124	ESO 3.6 m	1998 Feb	1200
WGAJ0747.0−6744	ESO 3.6 m	1999 Mar	1800	WGAJ1506.6−4008	ESO 2.2 m	1997 May	900
WGAJ0829.5+0858	ESO 3.6 m	1998 Feb	1800	WGAJ1507.9+6214	KPNO 4 m	1999 Feb	1200
WGAJ0847.2+1133	ESO 2.2 m	1997 May	900	WGAJ1509.5−4340	ESO 2.2 m	1997 May	1800
WGAJ0853.0+2004	ESO 3.6 m	1998 Feb	300	WGAJ1539.1−0658	ESO 3.6 m	1998 Feb	900
WGAJ0908.2+5031	KPNO 4 m	1999 Feb	1200	WGAJ1543.6+1847	ESO 2.2 m	1997 May	1200
WGAJ0927.7−0900	KPNO 4 m	1999 Feb	1800	WGAJ1606.0+2031	KPNO 2.1 m	1998 Jun	1800
WGAJ0931.9+5533	KPNO 4 m	1999 Feb	1200	WGAJ1610.3−3958	ESO 2.2 m	1997 May	1500
WGAJ0937.1+5008	KPNO 4 m	1999 Feb	600	WGAJ1626.6+5809	KPNO 2.1 m	1998 Jun	1200
WGAJ1006.1+3236	ESO 2.2 m	1997 May	900	WGAJ1629.7+2117	ESO 2.2 m	1997 May	1800
WGAJ1006.5+0509	ESO 2.2 m	1997 May	1800	WGAJ1648.4+4104	KPNO 2.1 m	1998 Jun	2700
WGAJ1010.8−0201	ESO 3.6 m	1998 Feb	900	WGAJ1656.6+5321	KPNO 4 m	1999 Feb	900
WGAJ1026.4+6746	KPNO 4 m	1999 Feb	1200	WGAJ1656.8+6012	KPNO 2.1 m	1998 Jun	2400
WGAJ1028.5−0236	ESO 3.6 m	1998 Feb	1200	WGAJ1722.3+3103	KPNO 2.1 m	1998 Jun	2400
WGAJ1028.6−0336	ESO 3.6 m	1999 Mar	1200	WGAJ1738.6−5333	ESO 2.2 m	1997 May	1200
WGAJ1056.9−7649	ESO 2.2 m	1997 May	2100	WGAJ1804.7+1755	ESO 3.6 m	1998 Sep	600
WGAJ1057.6−7724	ESO 3.6 m	1999 Mar	1200	WGAJ1808.2−5011	ESO 3.6 m	1999 Mar	1800
WGAJ1101.8+6241	KPNO 4 m	1999 Feb	1200	WGAJ1826.1−3650	ESO 3.6 m	1998 Sep	3600
WGAJ1105.3−1813	ESO 2.2 m	1997 May	1200	WGAJ1827.1−4533	ESO 3.6 m	1998 Sep	1200
WGAJ1116.1+0828	ESO 2.2 m	1997 May	1200	WGAJ1834.4−5856	ESO 3.6 m	1999 Mar	1800
WGAJ1120.4+5855	KPNO 4 m	1999 Feb	600	WGAJ1837.7−5848	ESO 2.2 m	1997 May	1800
WGAJ1204.2−0710	KPNO 2.1 m	1998 Jun	1200	WGAJ1840.9+5452	KPNO 2.1 m	1998 Jun	2700
WGAJ1206.2+2823	ESO 2.2 m	1997 May	1200	WGAJ1911.8−2102	ESO 3.6 m	1999 Mar	1800
WGAJ1213.0+3248	ESO 2.2 m	1997 May	1200	WGAJ1936.8−4719	ESO 3.6 m	2000 Aug	1200
WGAJ1213.2+1443	ESO 2.2 m	1997 May	1200	WGAJ2109.7−1332	KPNO 2.1 m	1998 Jun	1800
WGAJ1217.1+2925	ESO 2.2 m	1997 May	1200	WGAJ2151.3−4233	ESO 2.2 m	1997 May	900
WGAJ1222.6+2934	KPNO 4 m	1999 Feb	1200	WGAJ2154.1−1501	ESO 2.2 m	1997 May	600
WGAJ1223.9+0650	ESO 2.2 m	1997 May	1800	WGAJ2159.3−1500	ESO 2.2 m	1997 May	600
WGAJ1225.5+0715	ESO 3.6 m	1998 Feb	1200	WGAJ2201.6−5646	ESO 2.2 m	1997 May	1200
WGAJ1229.5+2711	KPNO 4 m	1999 Feb	1200	WGAJ2239.7−0631	ESO 3.6 m	1999 Aug	600
WGAJ1311.3−0521	ESO 3.6 m	1999 Mar	900	WGAJ2320.6+0032	ESO 3.6 m	1999 Aug	900
WGAJ1314.0−3304	ESO 2.2 m	1997 May	900	WGAJ2329.0+0834	ESO 3.6 m	1998 Sep	1800
WGAJ1315.1+2841	KPNO 4 m	1999 Feb	2700	WGAJ2330.6−3724	ESO 3.6 m	2000 Aug	900

3.2 Source Classification

The original definition of the blazar class (cf. Angel & Stockman 1980) emphasized the dominance of a highly polarized, variable, nonthermal continuum over other properties. The requirements for the classification as a blazar have nevertheless changed over the years (see Paper I). A flat radio spectrum, which is a direct indicator of radio core dominance (Impey & Tapia 1990), and an optical spectrum dominated by a non-thermal continuum and showing strong, broad emission lines or very weak features (see below), are currently the properties an identification as a blazar is based upon.

The blazar class is split into two subclasses: the flat spectrum radio quasars (FSRQ) and the BL Lacertae objects (BL Lacs). Both are believed to be radio galaxies with their jets viewed at small angles with respect to the line of sight, with BL Lacs and FSRQ being the "beamed" version of the Fanaroff-Riley (FR: Fanaroff & Riley 1974) type I and II radio galaxies (low- and high-radio power) respectively (e.g., Urry & Padovani 1995).

As the optical spectrum of a blazar is one of the main observational bases for its classification, it is important to understand its makeup. Three components seem to be present: synchrotron emission coming from the jet; broad and narrow lines emitted from clouds of different densities and temperatures orbiting the central engine of the active galaxy; and thermal stellar emission and absorption from the AGN host galaxy. Which of these components is actually observed in the spectrum of a radio-loud AGN appears to depend on the inclination of the jet with respect to the observer's line of sight.

If the jet forms a relatively large angle with the observer's line of sight, the broad line region (BLR), which is situated within a few parsecs of the central black hole, is thought to be obscured by the dusty torus assumed to surround the central engine (if the torus is roughly perpendicular to the jet). Therefore, only the narrow lines emitted from low-ionization clouds in the outer regions of the nucleus are detected in the optical spectrum. Furthermore, the synchrotron emission from the jet is barely visible and the host galaxy emission dominates. In the DXRBS an object exhibiting this kind of spectrum is classified as a Narrow Line Radio Galaxy (NLRG).

A change in the orientation of the jet brings the BLR into sight and leads, since relativistic effects also take place, to an increase of the jet synchrotron component. A source exhibiting both broad and narrow lines is classified in the DXRBS as a quasar. A dividing value of the full width at half maximum of 1000 km/s is adopted for quantifying the terms "narrow" and "broad." The transition in the orientation of the galaxy from larger to smaller angles is mirrored in a decrease of the value of the radio spectral index (Orr & Browne 1982). Based on this, a distinction between steep spectrum radio quasars (SSRQ) ($\alpha_r \gtrsim 0.5$) and flat spectrum radio quasars (FSRQ) ($\alpha_r \lesssim 0.5$) is made. A limit of 0.5 is generally chosen, since radio sources become increasingly core-dominated below this value. Note that for the identifications published in Paper I we chose to use a cut at $\alpha_r = 0.70$ to separate FSRQ and SSRQ. In this paper we follow the commonly accepted division at $\alpha_r = 0.50$. However, in the future we plan to refine this separation by using morphological, variability, and polarization information.

So far, there is no clear evidence for a stable BLR in FR I galaxies. Therefore, the face-on version of these objects, which are classified as BL Lacs, exhibit only weak narrow lines, if any at all. Broad lines have been observed in the spectra of a few objects of this class, but only temporarily (e.g., Vermeulen et al. 1995; Corbett et al. 1996).

Therefore, both BL Lac objects and NLRG show typically only narrow emission lines. To distinguish between these two classes of objects, we adopt in this publication the Marchã et al. (1996) definition. These authors base their criterion for an object to be classified as either a BL Lac or a radio galaxy on the value of the Ca break, a stellar absorption feature in the optical spectrum defined by $C = (f_+ - f_-)/f_+$ (where f_- and f_+ are the fluxes in the rest frame wavelength regions $3750 - 3950$ Å and $4050 - 4250$ Å respectively) and the equivalent width (EW) of the strongest emission line. In their Fig. 6 Marchã et al. show that objects in a triangular area limited by Ca break (contrast) $C = 0.4$ and a diagonal line (which assumes the line and continuum emission of the BL Lac object 3C 371 as its starting point and a smoothly decreasing AGN contribution) should be called BL Lacs. Candidates with narrow emission lines and $C > 0.4$, and therefore falling outside this region, are suggested to be classified as NLRG.

3.3 Optical Spectra

In the Appendix, we present the spectra of the optical counterparts. All spectra have been smoothed with Gaussian curves of width 3 pixels.

Of the 102 newly identified sources 86 are quasars (FSRQ and SSRQ) and 10 are BL Lacs. Adding the identifications published in Paper I, our technique is $\approx 90\%$ efficient at selecting radio-loud quasars and BL Lacs.

Nine objects in this publication are classified as radio galaxies. Note that these are sources with a relatively flat radio spectral index and therefore their jets are expected to be oriented closer to the line of sight than the ones with steeper α_r (> 0.7), typical of lobe dominated radio galaxies.

Stars have not been detected in the DXRBS. This is due to their weak radio emission (Helfand et al. 1999) with average fluxes below the limits of the radio catalogues employed in our survey.

Classifications, redshifts and their uncertainties, along with other observational properties for the objects presented here are given in Table 5. Column (1) gives the WGA name of the source whereas columns (2) and (3) give the *ROSAT* count rate and hardness ratio, respectively. The latter is the ratio between the count rates in the hard ($0.87 - 2.0$ keV) and medium ($0.4 - 0.86$ keV) bands (see Padovani & Giommi 1996 for details). Columns (4) and (5) give the 0.1 - 2.0 keV X-ray flux (not corrected for galactic extinction) and the unabsorbed X-ray flux at 1 keV respectively. Both X-ray fluxes have been derived from the *ROSAT* count rates using the observed hardness ratio and assuming galactic N_H. For objects observed more than once by *ROSAT*, we give the count rates, hardness ratios, and X-ray fluxes found for each observation. Column (6) gives the ratio between the $0.3 - 3.5$ keV X-ray flux and the radio flux at 6 cm, columns (7) and (8) give the radio flux at 6 cm and radio spectral index, the latter derived as described in § 2.2. Columns (9), (10) and (11) give the magnitudes in the B_j (from COSMOS), and O and E (from APM) spectral bands. For most of the faint objects the magnitude comes from other sources (see footnotes to table). The classification and redshift of the object

Table 4. Positional Information

Name	WGACAT Position RA	DEC	PSPC Center Offset [arcmin]	PMN or GB6 Position RA	DEC	Optical Position RA	DEC	Offset (X−O) [arcsec]	Offset/ Error
(1)	(2)	(3)	(4)	(5)	(6)	(7)	(8)	(9)	(10)
WGAJ0010.5−3027	00 10 33.7	−30 27 14	47.4	00 10 33.5	−30 27 31	00 10 35.7	−30 27 46	41.1	1.0
WGAJ0014.5−3059	00 14 34.1	−30 59 22	37.8	00 14 35.8	−30 59 08	00 14 38.0	−30 59 19	50.2	1.4
WGAJ0034.4−2133	00 34 29.9	−21 33 24	9.1	00 34 30.5	−21 34 03	00 34 30.9	−21 33 53	32.2	2.3
WGAJ0106.7−1034	01 06 43.1	−10 34 03	36.1	01 06 43.6	−10 34 26	01 06 44.1	−10 34 10	16.3	0.4
WGAJ0126.2−0500	01 26 13.6	−05 00 49	28.8	01 26 09.1	−05 00 40	01 26 15.0	−05 01 23	39.9	1.4
WGAJ0227.5−0847	02 27 32.1	−08 47 35	37.3	02 27 32.6	−08 47 59	02 27 32.1	−08 48 13	38.0	1.0
WGAJ0251.9−2051	02 51 55.2	−20 51 42	15.4	02 51 55.9	−20 52 18	02 51 54.9	−20 51 49[a]	8.2	0.4
WGAJ0305.3−2420	03 05 20.2	−24 20 39	29.5	03 05 20.9	−24 21 55	03 05 19.5	−24 21 34	55.8	1.9
WGAJ0307.7−4717	03 07 42.6	−47 17 20	33.4	03 07 38.2	−47 17 32	03 07 39.9	−47 17 43	35.8	1.0
WGAJ0322.1−5205	03 22 08.7	−52 05 32	17.9	03 22 11.5	−52 06 37	03 22 07.9	−52 05 36	8.4	0.5
WGAJ0322.6−1335	03 22 37.8	−13 35 15	12.1	03 22 39.2	−13 35 33	03 22 38.5	−13 35 18	10.6	0.6
WGAJ0421.5+1433	04 21 33.4	+14 33 44	11.8	04 21 33.1	+14 33 43	04 21 33.1	+14 33 54[b]	10.9	0.6
WGAJ0427.2−0756	04 27 13.7	−07 56 01	24.2	04 27 17.9	−07 56 37	04 27 14.2	−07 56 24	24.2	0.8
WGAJ0438.7−4727	04 38 45.3	−47 27 51	23.1	04 38 47.4	−47 28 16	04 38 47.0	−47 28 01	19.9	0.7
WGAJ0513.8+0156	05 13 52.3	+01 56 59	14.9	05 13 52.7	+01 56 50	05 13 51.8	+01 56 29[c]	30.6	1.7
	05 13 52.3	+01 56 59	14.9	05 13 52.7	+01 56 50	05 13 49.4	+01 55 52[c]	79.9	1.7
	05 13 53.4	+01 56 21	14.3	05 13 52.7	+01 56 50	05 13 51.8	+01 56 29	25.3	1.4
	05 13 53.4	+01 56 21	14.3	05 13 52.7	+01 56 50	05 13 49.4	+01 55 52	66.6	1.4
WGAJ0528.5−5820	05 28 34.7	−58 20 12	33.4	05 28 33.2	−58 20 25	05 28 34.9	−58 20 20	8.2	0.2
WGAJ0533.7−5817	05 33 45.2	−58 17 46	18.9	05 33 43.3	−58 17 41	05 33 45.3	−58 18 02	16.0	0.9
WGAJ0534.9−6439	05 34 58.7	−64 39 02	2.1	05 35 01.1	−64 38 35	05 35 00.2	−64 38 57	10.8	0.8
WGAJ0646.8+6807	06 46 49.8	+68 07 46	29.1	06 46 41.3	+68 07 40	06 46 42.4	+68 07 41[d]	41.7	1.4
WGAJ0651.9+6955	06 51 56.3	+69 55 35	34.8	06 51 55.2	+69 55 16	06 51 54.6	+69 55 26	12.6	0.3
WGAJ0741.7−5304	07 41 42.2	−53 04 42	29.4	07 41 49.6	−53 05 16	07 41 49.8	−53 04 39	68.5	2.4
WGAJ0747.0−6744	07 47 03.6	−67 44 41	7.1	07 46 55.7	−67 44 57	07 47 05.0	−67 44 41	8.0	0.6
WGAJ0829.5+0858	08 29 30.4	+08 58 25	26.4	08 29 29.9	+08 58 19	08 29 30.3	+08 58 21	4.3	0.1
WGAJ0847.2+1133	08 47 13.0	+11 34 30	48.1	08 47 10.3	+11 34 24	08 47 12.9	+11 33 50	40.0	1.0
WGAJ0853.0+2004	08 53 02.3	+20 04 34	23.6	08 53 03.1	+20 04 22	08 53 02.7	+20 04 22	13.2	0.5
	08 53 02.7	+20 04 23	23.5	08 53 03.1	+20 04 22	08 53 02.7	+20 04 22	1.0	0.0
WGAJ0908.2+5031	09 08 17.4	+50 31 10	19.5	09 08 16.3	+50 31 06	09 08 16.9	+50 31 05	6.9	0.4
WGAJ0927.7−0900	09 27 44.9	−09 00 28	22.7	09 27 48.9	−09 01 04	09 27 46.9	−09 00 22	30.2	1.1
WGAJ0931.9+5533	09 31 58.2	+55 33 45	24.1	09 32 00.8	+55 33 34	09 32 00.2	+55 33 46[e]	17.0	0.6
WGAJ0937.1+5008	09 37 10.9	+50 08 54	32.0	09 37 11.9	+50 08 44	09 37 12.3	+50 08 52	13.6	0.4
	09 37 11.2	+50 09 02	31.9	09 37 11.9	+50 08 44	09 37 12.3	+50 08 52	14.6	0.4
	09 37 12.1	+50 09 02	24.4	09 37 11.9	+50 08 44	09 37 12.3	+50 08 52	10.2	0.4
	09 37 12.1	+50 08 53	25.5	09 37 11.9	+50 08 44	09 37 12.3	+50 08 52	2.2	0.1
	09 37 13.6	+50 08 56	24.4	09 37 11.9	+50 08 44	09 37 12.3	+50 08 52	13.1	0.5
WGAJ1006.1+3236	10 06 08.3	+32 36 22	46.2	10 06 07.1	+32 36 20	10 06 07.7	+32 36 28	9.7	0.2
WGAJ1006.5+0509	10 06 34.1	+05 09 46	35.4	10 06 37.9	+05 09 50	10 06 37.6	+05 09 54	52.9	1.5
WGAJ1010.8−0201	10 10 52.6	−02 01 45	40.8	10 10 52.6	−02 00 57	10 10 51.6	−02 02 27	44.6	1.1
WGAJ1026.4+6746	10 26 29.1	+67 46 49	40.3	10 26 33.2	+67 46 02	10 26 34.0	+67 46 12	46.3	1.1
WGAJ1028.5−0236	10 28 33.2	−02 36 49	38.6	10 28 34.3	−02 37 12	10 28 34.1	−02 36 60	17.4	0.5
WGAJ1028.6−0336	10 28 39.4	−03 36 52	35.6	10 28 39.5	−03 35 57	10 28 40.4	−03 36 19	36.2	1.0
WGAJ1056.9−7649	10 56 54.3	−76 49 09	51.3	10 56 57.0	−76 49 23	10 56 54.6	−76 48 35	34.0	0.6
WGAJ1057.6−7724	10 57 41.0	−77 24 13	26.7	10 57 31.1	−77 24 24	10 57 33.4	−77 24 29	29.6	1.0
WGAJ1101.8+6241	11 01 53.2	+62 41 20	39.6	11 01 53.9	+62 41 55	11 01 53.4	+62 41 50[f]	30.0	0.8
WGAJ1105.3−1813	11 05 18.9	−18 13 06	25.0	11 05 15.2	−18 13 04	11 05 19.2	−18 13 13	8.2	0.3
WGAJ1116.1+0828	11 16 08.9	+08 28 14	50.5	11 16 10.2	+08 29 19	11 16 10.0	+08 29 22	69.9	1.3
WGAJ1120.4+5855	11 20 26.2	+58 55 57	18.4	11 20 27.7	+58 56 22	11 20 27.4	+58 56 12	17.6	1.0
	11 20 27.3	+58 56 19	16.3	11 20 27.7	+58 56 22	11 20 27.4	+58 56 12	7.0	0.4
WGAJ1204.2−0710	12 04 16.1	−07 10 03	34.6	12 04 16.8	−07 10 34	12 04 16.7	−07 10 10	11.3	0.3
WGAJ1206.2+2823	12 06 17.5	+28 23 19	35.7	12 06 20.5	+28 23 02	12 06 19.7	+28 22 54	38.3	1.1
WGAJ1213.0+3248	12 13 03.8	+32 48 00	34.9	12 13 04.3	+32 47 42	12 13 03.8	+32 47 37	23.0	0.6
WGAJ1213.2+1443	12 13 14.0	+14 43 47	43.5	12 13 16.6	+14 44 14	12 13 14.9	+14 44 00	18.4	0.4
WGAJ1217.1+2925	12 17 09.3	+29 25 28	29.2	12 17 08.6	+29 25 56	12 17 08.3	+29 25 32	13.7	0.5
WGAJ1222.6+2934	12 22 39.5	+29 34 40	41.9	12 22 42.4	+29 34 39	12 22 43.1	+29 34 41	47.0	1.1
	12 22 42.5	+29 34 54	20.1	12 22 42.4	+29 34 39	12 22 43.1	+29 34 40	16.0	0.6
WGAJ1223.9+0650	12 23 53.2	+06 50 13	31.2	12 23 54.7	+06 50 13	12 23 54.7	+06 50 02	24.9	0.7

Table 4 – *continued*

Name	WGACAT Position RA	DEC	PSPC Center Offset [arcmin]	PMN or GB6 Position RA	DEC	Optical Position RA	DEC	Offset (X−O) [arcsec]	Offset/ Error
(1)	(2)	(3)	(4)	(5)	(6)	(7)	(8)	(9)	(10)
WGAJ1225.5+0715	12 25 30.8	+07 15 59	18.1	12 25 30.8	+07 15 49	12 25 31.2	+07 15 52	9.2	0.5
WGAJ1229.5+2711	12 29 29.0	+27 12 21	40.4	12 29 33.3	+27 11 57	12 29 34.3	+27 11 57	74.7	1.8
WGAJ1311.3−0521	13 11 22.3	−05 21 16	30.1	13 11 21.2	−05 21 05	13 11 17.8	−05 21 22	67.5	1.9
WGAJ1314.0−3304	13 14 03.0	−33 04 04	12.8	13 14 04.5	−33 03 07	13 14 03.4	−33 03 56	9.4	0.5
WGAJ1315.1+2841	13 15 10.3	+28 41 12	30.1	13 15 13.9	+28 40 59	13 15 13.6	+28 40 53	47.4	1.3
WGAJ1320.4+0140	13 20 26.5	+01 40 37	16.1	13 20 27.1	+01 40 48	13 20 26.8	+01 40 36	4.6	0.3
WGAJ1323.8−3653	13 23 47.5	−36 53 06	28.9	13 23 46.0	−36 52 58	13 23 45.9	−36 53 39	38.2	1.3
WGAJ1329.0+5009	13 29 00.8	+50 09 39	38.5	13 29 06.0	+50 09 21	13 29 05.8	+50 09 26	49.8	1.4
WGAJ1332.7+4722	13 32 46.0	+47 22 32	32.2	13 32 45.7	+47 22 26	13 32 45.3	+47 22 22	12.3	0.3
WGAJ1333.1−3323	13 33 07.2	−33 23 52	23.2	13 33 06.4	−33 24 18	13 33 08.9	−33 24 39	51.6	1.8
WGAJ1337.2−1319	13 37 13.1	−13 19 03	23.5	13 37 16.4	−13 19 04	13 37 14.9	−13 19 17	29.8	1.0
WGAJ1353.2−4720	13 53 14.9	−47 20 56	22.2	13 53 15.4	−47 20 53	13 53 16.7	−47 20 55	18.3	0.6
WGAJ1359.6+4010	13 59 36.1	+40 10 54	27.1	13 59 37.5	+40 11 42	13 59 38.1	+40 11 38	49.6	1.7
WGAJ1400.7+0425	14 00 46.4	+04 25 51	21.0	14 00 48.5	+04 25 33	14 00 48.4	+04 25 31	36.0	1.3
WGAJ1402.7−3334	14 02 43.5	−33 34 01	25.3	14 02 41.0	−33 34 59	14 02 41.4	−33 34 09	27.4	0.9
WGAJ1404.2+3413	14 04 15.8	+34 13 21	29.0	14 04 16.7	+34 13 13	14 04 16.7	+34 13 16	12.2	0.4
WGAJ1406.9+3433	14 06 54.4	+34 33 42	21.2	14 06 54.0	+34 33 28	14 06 53.9	+34 33 37	8.0	0.3
WGAJ1416.4+1242	14 16 26.8	+12 42 47	40.0	14 16 28.3	+12 42 26	14 16 28.6	+12 42 13	43.0	1.0
	14 16 28.3	+12 42 18	26.5	14 16 28.3	+12 42 26	14 16 28.6	+12 42 13	6.7	0.2
WGAJ1417.5+2645	14 17 30.2	+26 45 12	8.6	14 17 30.6	+26 45 07	14 17 30.4	+26 44 57	15.2	1.1
WGAJ1419.1+0603	14 19 09.6	+06 03 49	26.6	14 19 09.2	+06 03 34	14 19 09.3	+06 03 30	19.5	0.7
WGAJ1420.6+0650	14 20 40.0	+06 50 58	32.1	14 20 40.9	+06 50 57	14 20 41.0	+06 50 58	14.9	0.4
	14 20 40.6	+06 51 04	32.3	14 20 40.9	+06 50 57	14 20 41.0	+06 50 58	6.3	0.2
WGAJ1423.3+4830	14 23 18.0	+48 30 06	14.1	14 23 18.4	+48 30 17	14 23 18.0	+48 30 16	10.0	0.5
WGAJ1427.9+3247	14 27 56.8	+32 47 44	25.9	14 27 58.3	+32 47 41	14 27 58.8	+32 47 40[g]	25.5	0.9
WGAJ1442.3+5236	14 42 21.3	+52 36 17	33.3	14 42 19.4	+52 36 20	14 42 19.6	+52 36 21	16.0	0.4
WGAJ1457.7−2818	14 57 42.0	−28 18 43	19.1	14 57 43.1	−28 19 19	14 57 44.6	−28 19 21	51.2	2.7
WGAJ1457.9−2124	14 57 55.3	−21 24 56	32.4	14 57 54.8	−21 25 08	14 57 54.1	−21 24 58	16.9	0.5
	14 57 55.3	−21 24 12	32.3	14 57 54.8	−21 25 08	14 57 54.1	−21 24 58	49.0	1.3
WGAJ1506.6−4008	15 06 36.0	−40 08 25	30.0	15 06 33.7	−40 07 35	15 06 37.2	−40 08 00	28.5	0.8
WGAJ1507.9+6214	15 07 55.9	+62 14 09	33.5	15 07 57.9	+62 13 44	15 07 57.3	+62 13 35	35.4	1.0
WGAJ1509.5−4340	15 09 35.8	−43 40 14	25.8	15 09 34.1	−43 40 41	15 09 35.7	−43 40 32	18.0	0.6
WGAJ1539.1−0658	15 39 09.8	−06 58 27	9.1	15 39 09.4	−06 58 29	15 39 09.6	−06 58 43	16.3	1.2
WGAJ1543.6+1847	15 43 40.7	+18 47 41	25.0	15 43 42.2	+18 47 07	15 43 43.8	+18 47 20	48.8	1.7
WGAJ1606.0+2031	16 06 05.3	+20 31 43	14.1	16 06 05.7	+20 32 14	16 06 05.9	+20 32 09	27.3	1.5
WGAJ1610.3−3958	16 10 20.5	−39 58 22	22.1	16 10 21.9	−39 58 59	16 10 21.9	−39 58 59	40.3	1.4
	16 10 21.1	−39 58 53	5.8	16 10 21.9	−39 58 59	16 10 21.9	−39 58 59	11.0	0.8
	16 10 22.1	−39 58 37	14.0	16 10 21.9	−39 58 59	16 10 21.9	−39 58 59	22.1	1.2
	16 10 23.9	−39 58 28	23.8	16 10 21.9	−39 58 59	16 10 21.9	−39 58 59	38.6	1.3
WGAJ1626.6+5809	16 26 37.3	+58 09 39	32.5	16 26 36.3	+58 09 14	16 26 37.4	+58 09 16	23.0	0.6
WGAJ1629.7+2117	16 29 47.0	+21 17 16	14.3	16 29 47.6	+21 17 22	16 29 47.7	+21 17 16	9.8	0.5
WGAJ1648.4+4104	16 48 28.3	+41 04 12	32.1	16 48 30.0	+41 04 07	16 48 29.3	+41 04 06	12.8	0.4
WGAJ1656.6+5321	16 56 41.8	+53 21 48	24.3	16 56 41.3	+53 21 51	16 56 39.7	+53 21 49	18.8	0.7
WGAJ1656.8+6012	16 56 41.7	+60 12 07	51.4	16 56 47.8	+60 12 28	16 56 48.3	+60 12 16	50.0	0.9
	16 56 48.1	+60 12 21	42.4	16 56 47.8	+60 12 28	16 56 48.3	+60 12 16	5.2	0.1
WGAJ1722.3+3103	17 22 19.7	+31 03 17	8.8	17 22 18.7	+31 03 29	17 22 19.0	+31 03 23	10.8	0.8
WGAJ1738.6−5333	17 38 37.5	−53 33 54	17.6	17 38 37.5	−53 34 05	17 38 38.8	−53 34 10	19.7	1.1
WGAJ1804.7+1755	18 04 42.8	+17 55 34	16.3	18 04 43.7	+17 55 36	18 04 42.5	+17 55 59	25.4	1.4
WGAJ1808.2−5011	18 08 13.0	−50 11 38	18.4	18 08 13.2	−50 11 55	18 08 13.9	−50 11 54	18.2	1.0
WGAJ1826.1−3650	18 26 07.4	−36 50 37	15.6	18 26 09.4	−36 51 12	18 26 08.1	−36 50 41	9.3	0.5
WGAJ1827.1−4533	18 27 09.9	−45 33 07	23.9	18 27 11.8	−45 33 02	18 27 10.2	−45 33 00	4.4	0.2
WGAJ1834.4−5856	18 34 27.3	−58 56 43	4.5	18 34 28.1	−58 56 35	18 34 27.5	−58 56 36	7.2	0.5
	18 34 27.3	−58 56 11	31.7	18 34 28.1	−58 56 35	18 34 27.5	−58 56 36	25.0	0.7
WGAJ1837.7−5848	18 37 44.9	−58 48 05	30.4	18 37 52.2	−58 48 14	18 37 53.8	−58 48 09	69.2	1.9
WGAJ1840.9+5452	18 40 58.2	+54 52 29	43.3	18 40 56.8	+54 52 29	18 40 57.4	+54 52 14	16.5	0.4
WGAJ1911.8−2102	19 11 50.6	−21 02 21	31.2	19 11 53.8	−21 02 49	19 11 54.1	−21 02 44	54.5	1.5

Table 4 – *continued*

Name	WGACAT Position RA	DEC	PSPC Center Offset [arcmin]	PMN or GB6 Position RA	DEC	Optical Position RA	DEC	Offset (X–O) [arcsec]	Offset/ Error
(1)	(2)	(3)	(4)	(5)	(6)	(7)	(8)	(9)	(10)
WGAJ1936.8−4719	19 36 53.1	−47 19 47	42.4	19 36 55.0	−47 19 38	19 36 56.1	−47 19 50	30.7	0.7
WGAJ2109.7−1332	21 09 47.0	−13 32 15	21.0	21 09 51.6	−13 32 59	21 09 49.9	−13 32 46	52.4	1.8
WGAJ2151.3−4233	21 51 20.6	−42 33 22	37.9	21 51 23.4	−42 33 41	21 51 21.9	−42 33 34	18.7	0.5
WGAJ2154.1−1501	21 54 06.2	−15 01 53	47.3	21 54 08.6	−15 01 54	21 54 07.5	−15 01 31[h]	27.2	0.6
	21 54 09.9	−15 02 12	47.7	21 54 08.6	−15 01 54	21 54 07.5	−15 01 31[h]	54.0	1.3
WGAJ2159.3−1500	21 59 18.7	−15 00 33	18.8	21 59 18.3	−15 00 40	21 59 20.2	−15 00 37	22.1	1.2
	21 59 20.1	−15 00 40	19.1	21 59 18.3	−15 00 40	21 59 20.2	−15 00 37	3.3	0.2
WGAJ2201.6−5646	22 01 37.5	−56 46 22	12.8	22 01 40.4	−56 46 45	22 01 38.4	−56 46 32	12.4	0.7
	22 01 37.6	−56 46 18	9.9	22 01 40.4	−56 46 45	22 01 38.4	−56 46 32	15.5	1.1
WGAJ2239.7−0631	22 39 46.5	−06 31 42	41.0	22 39 48.8	−06 31 48	22 39 46.9	−06 31 51[i]	10.8	0.3
WGAJ2320.6+0032	23 20 38.5	+00 32 17	31.9	23 20 39.1	+00 31 16	23 20 38.0	+00 31 39	38.7	1.1
WGAJ2329.0+0834	23 29 04.0	+08 34 51	22.0	23 29 05.5	+08 34 06	23 29 05.8	+08 34 15	44.8	1.6
WGAJ2330.6−3724	23 30 36.9	−37 24 30	35.1	23 30 36.9	−37 24 43	23 30 35.8	−37 24 36	14.4	0.4

[a] WGAJ0251.9−2051: optical counterpart 7″ off NVSS position
[b] WGAJ0421.5+1433: optical counterpart 9″ off NVSS position; NVSS source extended
[c] WGAJ0513.8+0156: three NVSS sources; the northermost optical counterpart is in between the two strongest sources, while the southernmost counterpart is 5″ off the faintest NVSS source. See § 3.4
[d] WGAJ0646.8+6807: optical counterpart 5″ off NVSS position
[e] WGAJ0931.9+5533: three NVSS sources; optical counterpart in between two of them; possible double-lobed source
[f] WGAJ1101.8+6241: optical counterpart 6″ off NVSS
[g] WGAJ1427.9+3247: two NVSS sources; optical counterpart in between them; possible double-lobed source
[h] WGAJ2154.1−1501: ATCA position; NVSS position 15″ off
[i] WGAJ2239.7−0631: optical counterpart 7″ off NVSS position

can be found in the last two columns, (12) and (13). The redshift was computed, whenever possible, by taking the mean of the values derived from the narrow lines. Where only a single (broad) emission line was observed, it was assumed to be Mg II λ2798 Å. When only weak features were present the redshift is marked as questionable in the table and the object is discussed individually. The redshift uncertainty represents the sample standard deviation. No error on the redshift is listed if only one emission line is present in the optical spectrum.

For objects which we classify as either radio galaxies or BL Lacs, we give the Ca break strength and the rest frame equivalent width of the strongest emission line in Table 6. Note that objects without a determined redshift have been excluded from this table, as well as WGAJ1120.4+5855, WGAJ1204.2−0710, and WGAJ1320.4+0140, for which the obtained spectrum does not cover the region of the Ca break. The error computation for the Ca break was based on the SNR blueward and redward of this feature.

Table 6. Spectral Characteristics of BL Lacs and Radio Galaxies

Name	Ca break	EW [Å]	Line
WGAJ0305.3−2420	?	25± 3	Hα
WGAJ0421.5+1433	0.51 ± 0.14	≤ 6	
WGAJ0528.5−5820	0.38 ± 0.18	26± 4	[O II]
WGAJ0847.2+1133	≤ 0.05	≤ 3	
WGAJ1056.9−7649	0.43 ± 0.35	32± 3	Hα
WGAJ1057.6−7724	0.48 ± 0.18	≤ 8	
WGAJ1229.5+2711	?	73±29	[O II]
WGAJ1311.3−0521	0.33 ± 0.12	≤ 2	
WGAJ1457.9−2124	0.45 ± 0.20	14± 2	Hα
WGAJ1840.9+5452	0.06 ± 0.12	8± 1	[O III]
WGAJ1936.8−4719	≤ 0.02	≤ 3	
WGAJ2151.3−4233	0.49 ± 0.22	6± 1	Hα
WGAJ2330.6−3724	0.10 ± 0.04	2± 1	[O III]

3.4 Notes on Individual Objects

WGAJ0305.3−2420 The Ca break for this object is located in noise and its measurement therefore impossible. Based on the relatively large equivalent width of its strongest line, we classify it as a radio galaxy, but note that a classification as a BL Lac cannot be excluded.

WGAJ0421.5+1433 Based on a newly acquired spectrum with a higher SNR than the one published in Paper I we determine the redshift for this object ($z = 0.059 \pm 0.001$) and reclassify it as a galaxy based on a Ca break value of 0.51±0.14. However, taking the error of the Ca break into account, a classification of this object as a BL Lac cannot be excluded.

WGAJ0513.8+0156 This is a problematic source. The (uncertain) BL Lac classification of this object given in Paper I was based on earlier information from the NVSS, which at that time listed only one radio source at the position given in Paper I. The error circle of the GB6 now in-

Table 5. Object Properties

Name	ROSAT		$F_{0.1-2.0keV}$	F_{1keV}	log	F_{6cm}	α_r	B_j	O	E	Class	z
	cts	hr	[erg/cm^2/s]	[μJy]	F_X/F_R	[mJy]						
(1)	(2)	(3)	(4)	(5)	(6)	(7)	(8)	(9)	(10)	(11)	(12)	(13)
WGAJ0010.5−3027	0.022	0.68	0.14E-12	0.011	−12.72	391	−0.15	19.1	19.5	18.8	FSRQ	1.19 ±0.01
WGAJ0014.5−3059	0.015	1.00	0.13E-12	0.022	−12.08	140	0.25	...	19.7	18.9	FSRQ	2.785±0.002
WGAJ0034.4−2133	0.003	2.60	0.26E-13	0.009	−12.17	82	0.56[a]	...	...	22.9[b]	SSRQ	0.764±0.001
WGAJ0106.7−1034	0.039	0.90	0.44E-12	0.091	−11.63	188	0.35	17.0	17.7	17.7	FSRQ	0.469±0.001
WGAJ0126.2−0500	0.027	1.25	0.31E-12	0.076	−11.19	54	0.21	18.3	...	...	FSRQ	0.411±0.001
WGAJ0227.5−0847	0.019	1.07	0.22E-12	0.051	−11.69	115	−0.34[c]	17.3	...	...	FSRQ	2.228±0.001
WGAJ0251.9−2051	0.015	1.67	0.13E-12	0.037	−11.45	53	0.65[d]	18.5	...	...	SSRQ	0.761
WGAJ0305.3−2420	0.013	0.67	0.10E-12	0.008	−12.25	102	−0.15	18.8	17.9	16.7	NLRG?	0.211±0.001
WGAJ0307.7−4717	0.024	0.93	0.22E-12	0.042	−11.76	123	0.70	23.2	...	...	SSRQ	0.599±0.001
WGAJ0322.1−5205	0.156	1.08	0.12E-11	0.262	−10.48	40	−0.27	16.8	...	...	FSRQ	0.416±0.001
WGAJ0322.6−1335	0.004	0.64	0.47E-13	0.008	−12.58	164	0.38	...	22.0[e]	...	FSRQ	1.468±0.001
WGAJ0421.5+1433	0.003	1.85	0.35E-13	0.017	−12.42	114	0.63	...	18.8	15.2	NLRG?	0.059±0.001
WGAJ0427.2−0756	0.012	1.29	0.14E-12	0.042	−11.52	56	0.27	21.0	...	...	FSRQ	1.375±0.003
WGAJ0438.7−4727	0.023	1.18	0.20E-12	0.041	−11.78	130	0.54	20.5	20.5	19.7	SSRQ	1.445±0.004
WGAJ0513.8+0156	0.031	3.47	0.42E-12	0.123	−11.26	131	0.45	...	...	14.3	NLRG	0.092±0.001
	0.023	2.37	0.30E-12	0.095	−11.49							
	0.031	3.47	0.42E-12	0.123	−11.26	131	0.45	...	...	17.7	NLRG	0.087±0.001
	0.023	2.37	0.30E-12	0.095	−11.49							
WGAJ0528.5−5820	0.014	1.09	0.14E-12	0.031	−11.80	99	0.70	18.7	17.8	16.7	BL Lac	0.254±0.001
*WGAJ0533.7−5817	0.009	1.70	0.11E-12	0.029	−11.68	66	0.94	17.9	18.5	18.4	SSRQ	0.757±0.001
*WGAJ0534.9−6439	0.016	1.63	0.21E-12	0.057	−11.48	76	0.77	20.5	...	...	SSRQ	1.463±0.001
WGAJ0646.8+6807	0.008	0.42	0.89E-13	0.009	−12.03	72	0.56	...	...	19.7[f]	SSRQ	0.927±0.001
WGAJ0651.9+6955	0.017	1.39	0.21E-12	0.067	−11.67	132	0.63	...	20.0	19.3	SSRQ	1.367
*WGAJ0741.7−5304	0.005	1.08	0.71E-13	0.024	−11.79	44	0.77	22.2	...	...	SSRQ	3.743±0.001
WGAJ0747.0−6744	0.005	1.25	0.68E-13	0.023	−11.59	27	0.16	19.7	...	...	FSRQ	1.025
WGAJ0829.5+0858	0.019	1.24	0.24E-12	0.058	−11.82	180	0.60	...	21.5[g]	...	SSRQ	0.866±0.001
*WGAJ0847.2+1133	1.290	1.20	0.16E-10	3.954	− 9.24	32	0.03	...	17.8	16.6	BL Lac	0.199±0.001
WGAJ0853.0+2004	0.010	1.20	0.86E-13	0.022	−11.73	60	0.60	...	18.2	18.0	SSRQ	1.930±0.003
	0.010	1.11	0.83E-13	0.019	−11.80							
WGAJ0908.2+5031	0.008	1.00	0.63E-13	0.010	−12.20	86	0.59	...	20.8	19.6	SSRQ	0.917
WGAJ0927.7−0900	0.014	1.86	0.20E-12	0.052	−11.82	181	−0.14	21.3	...	...	FSRQ	0.254±0.001
WGAJ0931.9+5533	0.045	1.25	0.43E-12	0.105	−11.00	53	0.66	...	16.7	16.0	SSRQ	0.266±0.001
*WGAJ0937.1+5008	0.056	1.00	0.51E-12	0.063	−11.95	315	−0.42	...	19.6	18.0	FSRQ	0.275±0.001
	0.069	1.64	0.74E-12	0.167	−11.52							
	0.056	1.73	0.53E-12	0.127	−11.64							
	0.072	1.67	0.67E-12	0.160	−11.53							
	0.058	1.20	0.50E-12	0.082	−11.85							
WGAJ1006.1+3236	0.052	0.71	0.43E-12	0.046	−11.91	231	0.62	...	18.7	18.1	SSRQ	1.02 ±0.01
WGAJ1006.5+0509	0.015	1.22	0.16E-12	0.037	−11.99	179	0.12	...	21.7	...	FSRQ	1.216±0.006
WGAJ1010.8−0201	0.063	0.90	0.82E-12	0.164	−12.02	826	0.32	18.9	19.9	18.9	FSRQ	0.896±0.002
WGAJ1026.4+6746	0.034	0.90	0.38E-12	0.069	−11.55	129	0.49	...	16.9[h]	17.9[h]	FSRQ	1.181
WGAJ1028.5−0236	0.019	1.16	0.24E-12	0.068	−11.53	94	−0.06	21.9	>22.0	19.6	FSRQ	0.476±0.002
*WGAJ1028.6−0336	0.008	0.58	0.76E-13	0.009	−11.99	61	0.74	19.1	20.5	...	SSRQ	1.781±0.001
WGAJ1056.9−7649	0.019	1.21	0.34E-12	0.113	−11.38	98	0.00	20.9	...	...	NLRG?	0.193±0.001
*WGAJ1057.6−7724	0.005	0.95	0.71E-13	0.020	−12.76	431	0.71	...	21.4[i]	...	NLRG?	0.181±0.001
WGAJ1101.8+6241	0.070	0.82	0.46E-12	0.038	−12.46	693	0.12	...	17.9	17.7	FSRQ	0.663±0.001
WGAJ1105.3−1813	0.006	1.50	0.80E-13	0.023	−11.77	59	−0.77	...	18.5	20.1	FSRQ	0.578±0.001
WGAJ1116.1+0828	0.014	1.26	0.22E-12	0.063	−11.98	282	−0.08	...	22.4[j]	...	FSRQ	0.486
*WGAJ1120.4+5855	0.008	0.96	0.60E-13	0.005	−12.19	46	0.61	...	18.5	16.0	NLRG	0.158±0.001
	0.026	1.46	0.21E-12	0.033	−11.40							
WGAJ1204.2−0710	0.058	0.76	0.45E-12	0.070	−11.50	128	0.22	18.0	...	...	BL Lac	0.185±0.001
*WGAJ1206.2+2823	0.013	0.31	0.89E-13	0.002	−11.96	21	0.41	...	19.5	18.9	FSRQ	0.708±0.002
WGAJ1213.0+3248	0.015	1.15	0.12E-12	0.022	−11.70	61	0.70	...	19.9	19.2	SSRQ	2.502±0.003
WGAJ1213.2+1443	0.044	1.06	0.48E-12	0.100	−11.08	61	0.50	...	21.0	19.9	FSRQ	0.718±0.002
*WGAJ1217.1+2925	0.012	0.92	0.94E-13	0.014	−11.80	49	0.27	...	19.9	19.2	FSRQ	0.974
WGAJ1222.6+2934	0.016	1.02	0.15E-12	0.029	−11.59	60	0.55	...	19.5	18.7	SSRQ	0.787±0.001
	0.016	1.33	0.15E-12	0.033	−11.54							
WGAJ1223.9+0650	0.018	1.01	0.18E-12	0.030	−12.18	251	0.11	...	21.2	...	FSRQ	1.189±0.003
WGAJ1225.5+0715	0.010	1.32	0.84E-13	0.016	−11.96	75	0.54	...	21.3	>20.0	SSRQ	1.12 ±0.01

Table 5 – *continued*

Name	ROSAT		$F_{0.1-2.0keV}$	F_{1keV}	log	F_{6cm}	α_r	B_j	O	E	Class	z
	cts	hr	[erg/cm^2/s]	[μJy]	F_X/F_R	[mJy]						
(1)	(2)	(3)	(4)	(5)	(6)	(7)	(8)	(9)	(10)	(11)	(12)	(13)
WGAJ1229.5+2711	0.024	1.67	0.28E-12	0.079	−11.56	165	0.16	...	>22.0	19.2	NLRG	0.490±0.001
WGAJ1311.3−0521	0.027	0.80	0.28E-12	0.040	−11.31	46	0.36	18.7	...	...	BL Lac	0.160±0.001
WGAJ1314.0−3304	0.026	1.64	0.33E-12	0.092	−11.50	125	0.50^k	19.3	...	...	FSRQ	0.484±0.001
WGAJ1315.1+2841	0.017	0.63	0.12E-12	0.008	−12.20	95	0.36	...	20.2	19.9	FSRQ	1.576±0.001
WGAJ1320.4+0140	0.022	1.41	0.20E-12	0.036	−12.46	541	0.01	20.8	20.8	>20.0	BL Lac	1.235±0.004
WGAJ1323.8−3653	0.007	0.76	0.92E-13	0.019	−12.18	135	−0.04	21.9	...	...	BL Lac?	?
WGAJ1329.0+5009	0.023	0.84	0.16E-12	0.018	−12.08	133	0.68	...	20.1	19.2	SSRQ	2.65 ±0.01
WGAJ1332.7+4722	0.033	1.06	0.33E-12	0.056	−12.05	333	0.54	...	19.3	18.9	SSRQ	0.668±0.001
WGAJ1333.1−3323	0.005	1.22	0.55E-13	0.014	−12.33	140	0.22	21.7	...	...	FSRQ	2.24 ±0.01
WGAJ1337.2−1319	0.022	1.22	0.32E-12	0.085	−11.30	71	0.38^l	...	19.8	18.8	FSRQ	3.475±0.003
WGAJ1353.2−4720	0.019	2.78	0.30E-12	0.128	−11.63	198	0.66	21.4	...	...	SSRQ	0.550±0.001
WGAJ1359.6+4010	0.014	1.20	0.13E-12	0.020	−12.41	281	−0.76	...	19.2	17.6	FSRQ	0.407±0.001
WGAJ1400.7+0425	0.009	0.63	0.80E-13	0.008	−12.73	267	0.06	...	21.3	...	FSRQ	2.55 ±0.01
WGAJ1402.7−3334	0.042	2.12	0.61E-12	0.172	−11.00	88	−0.02	23.0	...	...	FSRQ	2.14 ±0.01
WGAJ1404.2+3413	0.011	1.07	0.78E-13	0.012	−11.98	62	0.67	...	18.6	17.6	SSRQ	0.937±0.002
WGAJ1406.9+3433	0.014	0.82	0.11E-12	0.010	−12.51	204	0.27	...	18.7	17.9	FSRQ	2.556±0.001
WGAJ1416.4+1242	0.100	0.56	0.95E-12	0.058	−11.36	98	0.30	...	18.1	17.7	FSRQ	0.335±0.001
	0.098	1.07	0.87E-12	0.148	−11.09							
WGAJ1417.5+2645	0.006	1.47	0.51E-13	0.010	−12.17	77	0.29	...	21.9	>20.0	FSRQ	1.455±0.005
WGAJ1419.1+0603	0.009	1.25	0.97E-13	0.022	−12.33	240	0.01	...	...	20.5^m	FSRQ	2.389±0.003
WGAJ1420.6+0650	0.028	1.26	0.33E-12	0.076	−11.80	241	0.56	...	...	17.5	SSRQ	0.236±0.001
	0.033	0.73	0.35E-12	0.042	−12.00							
WGAJ1423.3+4830	0.022	1.46	0.20E-12	0.037	−11.72	100	0.55	...	19.4	19.1	SSRQ	0.569±0.001
WGAJ1427.9+3247	0.052	0.99	0.38E-12	0.055	−11.32	65	0.66	...	18.1	17.6	SSRQ	0.568±0.001
WGAJ1442.3+5236	0.016	1.35	0.14E-12	0.036	−11.77	111	0.32	...	19.3	18.5	FSRQ	1.80 ±0.01
∗WGAJ1457.7−2818	0.007	0.67	0.89E-13	0.019	−12.19	136	0.40^n	18.8	...	...	FSRQ	1.999±0.001
WGAJ1457.9−2124	0.035	1.19	0.54E-12	0.166	−11.38	146	0.79	21.3	21.6	18.3	NLRG	0.319±0.001
	0.040	1.21	0.61E-12	0.191	−11.32							
WGAJ1506.6−4008	0.018	0.68	0.27E-12	0.064	−11.60	110	0.10	...	19.6^o	...	FSRQ	1.031±0.002
WGAJ1507.9+6214	0.018	0.56	0.12E-12	0.008	−12.52	213	0.69	...	18.5	18.1	SSRQ	1.478±0.001
WGAJ1509.5−4340	0.016	1.07	0.24E-12	0.081	−11.83	165	−0.40	19.2	...	...	FSRQ	0.776±0.001
WGAJ1539.1−0658	0.005	0.94	0.70E-13	0.018	−12.03	76	−0.27	20.0	...	...	BL Lac?	?
WGAJ1543.6+1847	0.011	1.33	0.13E-12	0.035	−12.26	300	0.13	...	19.5	18.8	FSRQ	1.396±0.006
WGAJ1606.0+2031	0.006	2.17	0.66E-13	0.018	−12.31	196	0.32	...	...	18.3	FSRQ	0.383±0.001
∗WGAJ1610.3−3958	0.026	3.75	0.40E-12	0.209	−12.09	882	0.19	20.9	...	...	FSRQ	0.518±0.001
	0.011	12.00	0.17E-12	0.086	−12.69							
	0.023	3.25	0.29E-12	0.165	−12.31							
	0.022	2.14	0.30E-12	0.208	−12.34							
WGAJ1626.6+5809	0.032	1.22	0.32E-12	0.067	−11.95	315	0.55	...	...	17.5	SSRQ	0.748±0.001
WGAJ1629.7+2117	0.013	1.38	0.14E-12	0.035	−11.81	105	0.50	...	21.5	>20.0	FSRQ	0.833±0.002
WGAJ1648.4+4104	0.061	1.11	0.61E-12	0.109	−11.54	197	0.52	...	19.8	19.0	SSRQ	0.851±0.001
WGAJ1656.6+5321	0.014	1.27	0.15E-12	0.033	−11.94	145	0.09	...	...	19.1^p	FSRQ	1.555
WGAJ1656.8+6012	0.032	0.66	0.29E-12	0.029	−11.99	184	−0.33	...	19.0^q	18.4^r	FSRQ	0.623±0.001
	0.032	0.38	0.23E-12	0.007	−12.37							
WGAJ1722.3+3103	0.014	1.38	0.16E-12	0.036	−11.50	53	0.58	...	21.2	18.7	SSRQ	0.305±0.001
WGAJ1738.6−5333	0.015	1.80	0.19E-12	0.072	−12.10	307	−0.10	...	18.4^r	...	FSRQ	1.721±0.001
WGAJ1804.7+1755	0.009	1.56	0.11E-12	0.036	−11.84	92	0.29	...	19.4	18.7	FSRQ	0.435±0.001
WGAJ1808.2−5011	0.011	1.27	0.14E-12	0.042	−12.44	425	−0.33	...	20.4^s	...	FSRQ	1.606±0.004
WGAJ1826.1−3650	0.016	1.72	0.20E-12	0.078	−12.35	552	−0.06	...	...	18.8^t	FSRQ	0.888
WGAJ1827.1−4533	0.023	1.16	0.33E-12	0.104	−12.09	451	0.00	18.1	...	...	FSRQ	1.244±0.001
WGAJ1834.4−5856	0.011	2.59	0.15E-12	0.046	−12.25	399	0.00	19.7	...	...	BL Lac	?
	0.023	0.95	0.35E-12	0.102	−12.03							
WGAJ1837.7−5848	0.012	0.80	0.19E-12	0.053	−12.02	211	−0.08	19.3	...	...	FSRQ	3.040±0.002
WGAJ1840.9+5452	0.040	1.33	0.58E-12	0.179	−11.53	252	0.39	...	19.4	18.8	BL Lac	0.646±0.001
WGAJ1911.8−2102	0.018	0.59	0.30E-12	0.084	−12.17	443	0.28	...	17.0^u	19.5^u	FSRQ	1.42 ±0.01
WGAJ1936.8−4719	0.202	1.36	0.34E-11	0.936	−10.17	60	−0.11	20.3	...	...	BL Lac	0.265±0.001
WGAJ2109.7−1332	0.014	1.01	0.16E-12	0.034	−11.49	51	0.16	19.3	18.2	17.8	FSRQ	1.226±0.001

Table 5 – *continued*

Name	ROSAT cts	ROSAT hr	$F_{0.1-2.0keV}$ [erg/cm^2/s]	F_{1keV} [μJy]	log F_X/F_R	F_{6cm} [mJy]	α_r	B_j	O	E	Class	z
(1)	(2)	(3)	(4)	(5)	(6)	(7)	(8)	(9)	(10)	(11)	(12)	(13)
WGAJ2151.3−4233	0.030	0.83	0.26E-12	0.031	−12.16	265	0.51^v	16.1^w	...	...	NLRG	0.061±0.001
WGAJ2154.1−1501	0.033	0.84	0.36E-12	0.072	−11.78	219	0.30	...	16.5	16.4	FSRQ	1.208±0.005
	0.033	1.06	0.35E-12	0.091	−11.71							
WGAJ2159.3−1500	0.005	1.46	0.49E-13	0.013	−12.16	86	0.01^x	18.2	18.9	18.4	FSRQ	2.270±0.010
	0.013	1.05	0.13E-12	0.027	−11.82							
∗WGAJ2201.6−5646	0.047	1.09	0.45E-12	0.077	−11.23	67	0.71	17.5	...	...	SSRQ	0.410±0.001
	0.022	1.47	0.22E-12	0.049	−11.44							
WGAJ2239.7−0631	0.069	1.31	0.97E-12	0.259	−10.72	64	0.54	...	20.1	18.8	SSRQ	0.264±0.001
WGAJ2320.6+0032	0.013	1.05	0.16E-12	0.036	−11.71	87	0.45	18.9	...	...	FSRQ	1.894±0.001
WGAJ2329.0+0834	0.004	2.67	0.61E-13	0.020	−12.35	273	0.06	...	20.5^y	...	FSRQ	0.948±0.001
WGAJ2330.6−3724	0.032	0.88	0.27E-12	0.038	−12.05	238	0.19	16.6	...	...	BL Lac	0.279±0.001

∗ Source does not meet strict DXRBS selection criteria
[a] WGAJ0034.4−2133: $\alpha_{\rm ATCA} = 1.91$
[b] WGAJ0034.4−2133: $V_{\rm mag}$ from ESO image
[c] WGAJ0227.5−0847: $\alpha_{\rm ATCA} = 0.36$
[d] WGAJ0251.9−2051: $\alpha_{\rm ATCA} = 1.70$
[e] WGAJ0322.6−1335: $V_{\rm mag}$ from ESO image
[f] WGAJ0646.8+6807: $R_{\rm mag}$ from WYIN image
[g] WGAJ0829.5+0858: $V_{\rm mag}$ from ESO image
[h] WGAJ1026.4+6746: two merged objects in APM: given magnitudes assume a flux ratio of ~ 2
[i] WGAJ1057.6−7724: $V_{\rm mag}$ from ESO image
[j] WGAJ1116.1+0828: $V_{\rm mag}$ from ESO image
[k] WGAJ1314.0−3304: $\alpha_{\rm ATCA} = 0.97$
[l] WGAJ1337.2−1319: $\alpha_{\rm ATCA} = 0.87$
[m] WGAJ1419.1+0603: $R_{\rm mag}$ from CTIO image
[n] WGAJ1457.7−2818: $\alpha_{\rm ATCA} = 0.72$, TEXAS survey double
[o] WGAJ1506.6−4008: $V_{\rm mag}$ from ESO image
[p] WGAJ1656.6+5321: $R_{\rm mag}$ from WYIN image
[q] WGAJ1656.8+6012: USNO magnitudes (two merged objects in APM)
[r] WGAJ1738.6−5333: $V_{\rm mag}$ from ESO image
[s] WGAJ1808.2−5011: $V_{\rm mag}$ from ESO image
[t] WGAJ1826.1−3650: $R_{\rm mag}$ from spectrum
[u] WGAJ1911.8−2102: USNO magnitudes
[v] WGAJ2151.3−4233: $\alpha_{\rm r}$ from PMN-Parkes data
[w] WGAJ2151.3−4233: magnitude from the APM Bright Galaxy Catalogue (Loveday 1996)
[x] WGAJ2159.3−1500: $\alpha_{\rm ATCA} = 1.46$
[y] WGAJ2329.0+0834: magnitude from DSS 2

cludes three NVSS sources. The object published in Paper I is next to the brightest one at $z = 0.084$. Further observations yielded two other galaxies at redshifts $z = 0.087$ and $z = 0.092$, the former close to the faintest NVSS source, the latter in between the two brightest radio sources. The similar redshifts of the observed galaxies suggest a small group. With the information available, it is currently impossible to say which object is the radio counterpart of the WGA source.

WGAJ0528.5−5820 We refine the redshift of this source to $z = 0.254 \pm 0.001$; however, the classification as a BL Lac is unaffected. The spectrum of a star close to the DXRBS candidate has been erroneously identified as the optical counterpart in Paper I.

WGAJ0847.2+1133 This object was identified independently by Cao et al. (1999). We confirm its identification and redshift.

WGAJ0937.1+5008 This object was identified independently by Henstock et al. (1997). We confirm its identification and redshift. Our spectrum, however, is significantly bluer and reflects a higher continuum level. As a result, the emission lines in our spectrum are correspondingly weaker.

WGAJ1056.9−7649 We classify this object as a galaxy, but given the large error on the Ca break we cannot exclude a classification as a BL Lac.

WGAJ1057.6−7724 This object was classified in Paper I as a BL Lac with an uncertain redshift of $z = 0.541$. A new spectrum obtained in March 1999 at ESO 3.6 m yields a reclassification of this source as a radio galaxy with a redshift of $z = 0.181 \pm 0.001$ and a Ca break value of 0.48±0.18. Note that the error in the contrast puts this object close to the dividing value of 0.4 adopted by Marchã et al. (1996) to distinguish radio galaxies from BL Lac objects.

WGAJ1101.8+6241 This object was identified independently by Henstock et al. (1997). We confirm its identification and redshift.

WGAJ1116.1+0828 The redshift for this object given in Table 5 refers to the emission line. The absorption system detected is at $z = 0.163 \pm 0.001$.

WGAJ1120.4+5855 The classification of this object as a NLRG is based on the rest-frame equivalent width of 40 Å for the strongest emission line [O III] $\lambda5007$ and is ambiguous without an information on the Ca break strength.

WGAJ1204.2−0710 The claimed redshift for this object is tentative due to the weakness of the identified absorption features.

WGAJ1222.6+2934 A newly acquired spectrum of this source allows a redetermination of the redshift to $z = 0.787 \pm 0.001$; however, the classification as an FSRQ is unaffected.

WGAJ1320.4+0140 The redshift given in Drinkwater et al. (1997) for this object coincides within the errors with the redshift determined from our spectrum. The strongest emission line C III] has a rest-frame equivalent width of 9 Å, therefore we classify this object as a BL Lac.

WGAJ1323.8−3653 We classify this faint object as a BL Lac, based on the absence of strong emission and absorption features. However, we cannot claim this object to be completely featureless, in particular above $\lambda \sim 7,000$ Å, because in that region the lower SNR renders the sky subtraction problematic.

WGAJ1329.0+5009 This object was identified independently by Falco, Kochanek, & Muñoz (1998). We confirm its identification and redshift.

WGAJ1420.6+0650 This source seems to be partially obscured. We detect a broad Hα emission line, but no Hβ emission is visible.

WGAJ1539.1−0658 We classify this object as a BL Lac, based on the absence of strong emission and absorption features. However, we cannot claim this object to be completely featureless, in particular above $\lambda \sim 7,000$ Å, because in that region the lower SNR renders the sky subtraction problematic.

WGAJ1656.6+5321 This object was identified independently by Falco, Kochanek, & Muñoz (1998). We confirm its identification and redshift.

4 SAMPLE PROPERTIES

As of July 2000*, 189 objects have been spectroscopically identified. Of these, 151 (80.0%) are quasars, 24 (12.6%) are BL Lacs, and 14 (7.4%) are NLRG. These numbers include 10 sources which have been observed as part of other surveys and whose classification was made available to us before publication. Another 109 previously known objects are also in the sample, of which 83 are quasars, 12 are BL Lacs, and 14 are NLRG. These numbers are larger than those reported in Paper I because of our expanded criteria, discussed in § 2. Our sample now contains 234 quasars (181 FSRQ and 53 SSRQ), 36 BL Lacs, and 28 NLRG, for a total of 298 identified sources. As a result of the observations presented here we have increased the number of newly identified objects in our sample by more than 50%. Table 7 summarizes the status of the identifications.

The subsample of sources which fulfill all our selection criteria [§ 2 and Paper I] and which will be used for the detailed analysis is now 85% identified. It includes 275 objects, of which 222 are quasars (175 FSRQ and 47 SSRQ), 31 are BL Lacs, and 22 are NLRG. An ESO Very Large Telescope (VLT) program to identify 15 very faint ($R \sim 23$) DXRBS candidates has been partially completed (data reduction is in progress); another such program is currently under way. Approximately 50 sources remain to be identified (about half of them have been observed during our ESO run in August 2000; data reduction is in progress). These sources are about one magnitude fainter than the rest of the DXRBS sample ($\langle V \rangle \sim 19.2$ as compared to 18.3). Based on our results so far, we expect them to be mostly quasars at relatively high ($z \gtrsim 1.5$) redshifts. With this in mind, we now review the properties of the sample.

4.1 Redshift Distributions

Figure 2 displays the fractional redshift distribution of the DXRBS quasars compared to the quasars found in the S4 ($f_{5\mathrm{GHz}} > 0.5$ Jy) and 1 Jy ($f_{5\mathrm{GHz}} > 1$ Jy) surveys (Stickel & Kühr 1994; Stickel, Meisenheimer & Kühr 1994). Note that DXRBS quasars have been selected to have $\alpha_r \leq 0.7$. Therefore the S4 and 1Jy distributions shown here comprise the quasars from these samples defined on the same basis.

While for the S4 and 1 Jy surveys the area of the sky covered is the same at all fluxes (5,624 and 32,208 deg^2 respectively), this is not the case for DXRBS. Due to the serendipitous nature of the survey and the variable sensitivity of the *ROSAT* PSPC detector across the field of view, the area in which faint X-ray sources could be detected is smaller than that for brighter X-ray sources. The DXRBS redshift distribution has therefore been de-convolved with the appropriate sky coverage and this is what is shown in Fig. 2. Namely, each bin represents $\sum 1/\mathrm{Area}(f_\mathrm{x})$ for all the sources in that bin, where $\mathrm{Area}(f_\mathrm{x})$ is the area accessible at its X-ray flux, divided by the total surface density of sources. Error bars represent the 1σ range based on Poisson statistics. We note that the sky coverage is difficult to determine in the parts of the PSPC field of view affected by the rib structure ($13' <$ offset $< 24'$). That area, and the sources within, have therefore been excluded from the analysis presented in this subsection. Moreover, only sources with $f_{5\mathrm{GHz}} > 51$ mJy have been included since we still not have computed the sky coverage of the PMN survey below this flux.

As the radio flux limit of the quasar samples drops from 1 Jy to $\sim$ 0.05 Jy, the approximate limit of the DXRBS, a progression towards higher redshifts is clearly seen, as expected. The mean redshift, in fact, moves from $\langle z \rangle = 1.18 \pm 0.05$ for the 1 Jy, to $\langle z \rangle = 1.30 \pm 0.07$ for the S4, to $\langle z \rangle = 1.56 \pm 0.06$ for the DXRBS sample. A Kolmogorov-

* We include here the spectra of two BL Lacs we reobserved in August 2000, as those spectra are of better quality than those we previously had.

Table 7. Sample Identification Status

Class	Newly identified		Previously known	Total		Uncertain Class	No z
Radio-Loud Quasars	151	139	83	234	222	0	0
BL Lacs	24	19	12	36	31	3	11
Radio Galaxies	14	8	14	28	22	4	0
Total	189	166	109	298	275	7	11

The numbers to the right in columns (2) and (4) refer to sources which fulfill all DXRBS selection criteria.

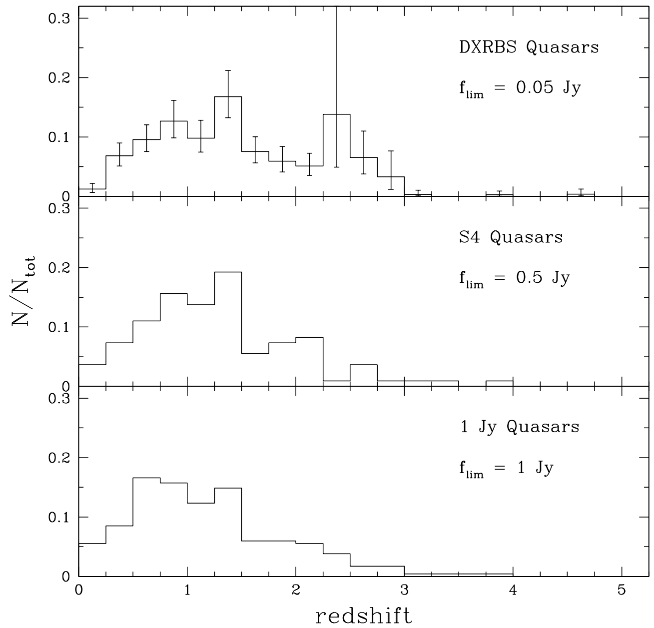

Figure 2. Fractional redshift distribution for the 148 DXRBS, 109 S4, and 235 1 Jy quasars with $\alpha_{\rm r} \leq 0.7$. The DXRBS distribution has been de-convolved with the appropriate sky coverage. Error bars represent the 1σ range based on Poisson statistics.

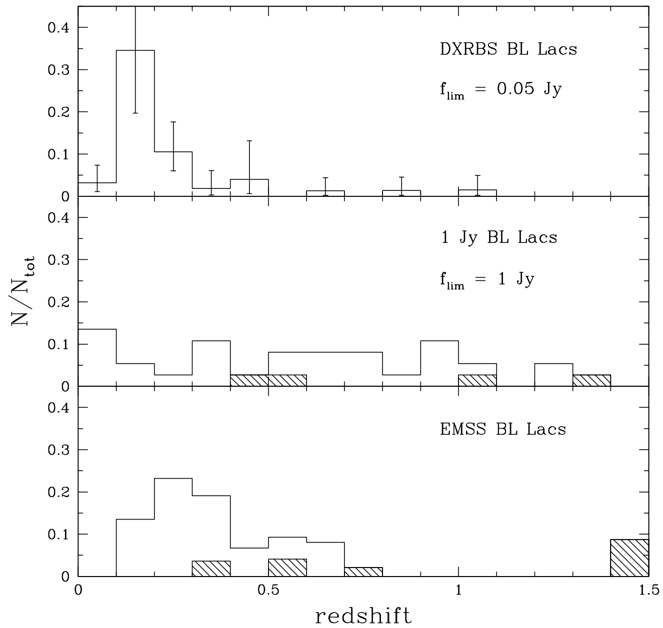

Figure 3. Fractional redshift distribution for the 17 DXRBS, 32 1 Jy, and 38 EMSS BL Lacs. The DXRBS and EMSS distributions have been de-convolved with the appropriate sky coverages. The hatched areas represent lower limits (1 Jy) and uncertain values (EMSS). Error bars represent the 1σ range based on Poisson statistics. See text for details.

Smirnov test shows that the DXRBS redshift distribution is significantly different ($P > 99\%$) from the 1 Jy and S4 distributions. The mean values are also different at the same significance level. Considering that the DXRBS quasar sample is $\sim 85\%$ complete and that the missing sources are likely to be at relatively high ($z \gtrsim 1.5$) redshift, we expect the final mean redshift to be even higher. Compared to the S4 and 1 Jy samples, a larger fraction of DXRBS quasars are at relatively high redshift. In fact, DXRBS finds $\sim 30\%$ of its quasars at $z > 2$ (once the effect of the WGACAT sky coverage is taken into account), whereas only $\sim 15\%$ of the S4 and 1 Jy quasars lie above this redshift.

Figure 3 displays the redshift distribution of the DXRBS BL Lacs, compared to that of the 1 Jy (Stickel et al. 1991; Stickel & Kühr 1994; Stocke & Rector 1997) and EMSS (Rector et al. 2000) samples. The DXRBS and EMSS redshift distributions have been de-convolved with the appropriate sky coverage (the sky coverage for the EMSS was taken from Gioia et al. 1990 and Morris, private communication). We have not included BL Lacs from the *Einstein* Slew Survey (Perlman et al. 1996a) in this plot because the sky coverage of that survey is not fully known yet. Five EMSS redshifts are uncertain, while four 1 Jy redshifts are lower limits (hatched areas in Fig. 3; five more 1 Jy sources have a lower limit on their redshift of 0.2 based on the non-detection of their host galaxies on the optical image). Note that the fraction of BL Lacs with redshift information ranges from 93% and 86% for the EMSS and 1 Jy samples respectively to 63% for DXRBS. Half of the DXRBS BL Lacs without a determined redshift are previously known objects, and therefore have not been spectroscopically observed by us.

The mean redshift for the three BL Lac samples is 0.24 for DXRBS, 0.46 for the EMSS, and 0.63 (including lower limits) for the 1 Jy. The DXRBS and EMSS samples are peaked at $z = 0.2$ and $z = 0.3 - 0.4$ respectively, and neither sample has significant numbers of $z > 0.8$ objects ($\sim 9\%$ in the EMSS and $\sim 12\%$ in the DXRBS). By comparison, the 1 Jy BL Lacs have an essentially flat redshift distribution out to nearly $z = 1.5$, with 10/32 1 Jy BL Lacs at $z > 0.8$ and 5 at $z > 1$. In contrast to the quasars, no progression to higher redshifts is seen for the BL Lacs as the radio flux limit drops from 1 Jy, for the 1 Jy sample, to 0.05 Jy for the DXRBS. Similarly, no progression of this kind is seen as the X-ray flux limit drops from a few $\times 10^{-13}$ erg cm^{-2} s^{-1} for the EMSS to a few $\times 10^{-14}$ erg cm^{-2} s^{-1} for the DXRBS. In this paper, however, we will not attempt a detailed comparison of the three BL Lac redshift distributions. At this stage, this would not be meaningful, first because, as mentioned above, about one third of the DXRBS BL Lacs are not included in Figure 3 since they lack redshifts, and second because the identification of DXRBS is not 100% complete yet. We would only like to note that the criteria employed to classify objects as a BL Lac were somewhat different in each of these surveys. As we previously pointed out in Paper I, while the spectroscopic criteria employed for DXRBS and the EMSS were identical (once the EMSS criteria were expanded to take into account the Marchã et al. (1996) expansion of the original BL Lac region in the (C, W_λ) plot; see Rector et al. 1999 for discussion), the EMSS did not require a flat radio spectrum to classify an X-ray source as a candidate BL Lac. The 1 Jy survey used a different set of criteria to classify objects as BL Lacs, requiring $\alpha_r \leq 0.5$ and $W_\lambda < 5(1 + z)$ Å but with no restriction on the Ca break. In addition, as was detailed in Paper I and Perlman et al. (1996b), the 1 Jy survey was often inconsistent in applying its selection criteria. Similar points have also been made by other authors (Marchã & Browne 1995; Stocke & Rector 1997; Rector, Stocke & Perlman 1999).

We note the striking difference in redshift range between BL Lacs and quasars, the latter reaching $z \sim 4.7$, the former only getting up to $z \sim 1.5$. Note that, while $\sim 37\%$ of DXRBS BL Lacs lack a redshift determination, that is not the case for the EMSS and 1 Jy samples for which redshifts are available for $\sim 90\%$ of the sources. Although one cannot exclude the possibility that the missing redshifts are all relatively high, the point remains that the mean redshift values for BL Lacs and quasars *belonging to the same sample* are significantly different.

Finally, the redshift distribution for the radio galaxies in our sample reaches only $z \sim 0.4$ and is skewed towards low redshifts, with $\langle z \rangle = 0.13$.

4.2 X-ray/Radio Luminosities

Because it reaches much lower fluxes than any previously published sample of FSRQ (by a factor $10 - 20$ in radio flux and by a factor 10 in X-ray flux), DXRBS has vastly expanded the coverage of parameter space for FSRQ in complete samples. These expansions occur in two regions of the $L_{\rm x}, L_{\rm r}$ plane: (1) at low luminosities; (2) at high $L_{\rm x}/L_{\rm r}$ values, with the discovery of a new class of X-ray bright FSRQ.

At the low luminosity end, DXRBS includes at present $\sim 5\times$ more FSRQ with $L_{\rm r} < 10^{26.5}$ W Hz^{-1} than the S4 and 1 Jy samples combined. About 40 DXRBS FSRQ are in fact already known at these low powers, and this will put strong constraints on the FSRQ radio luminosity function (LF). For comparison, note that the radio LF derived by Urry & Padovani (1995) from the 2 Jy sample (the only published high frequency sample with relatively complete redshift information) included only one source at $L_{\rm r} < 10^{26.5}$ W Hz^{-1}, a power which coincides roughly with the predicted flattening of the LF based on unified schemes. Five of these low-power objects are in a luminosity range never before reached for FSRQ: $10^{24.5} < L_{\rm r} < 10^{25.5}$ W Hz^{-1}, the former being the expected minimum luminosity of FSRQ assuming these objects are beamed FR II radio galaxies.

Paper I discussed the finding of a large fraction ($\sim 25\%$) of X-ray bright ($\log L_{\rm x}/L_{\rm r} > -6$ or $\alpha_{\rm rx} < 0.78$) FSRQ in the DXRBS, and termed them high-energy peaked FSRQ (HFSRQ), stressing the similarity in their broadband spectral shapes to the high-energy peaked BL Lacs. The fraction of HFSRQ in the DXRBS is now 28%. We also find 14 high-energy peaked SSRQ. By comparison, the previously known complete samples included very few of these objects (3% in total). As discussed in Paper I, the reason for this discrepancy is because DXRBS is the first X-ray survey which included the radio spectral slope in its identification process, thus for the first time allowing the identification of a sample of X-ray emitting FSRQ. Importantly, further research on other samples has shown that the X-ray/radio luminosity distribution of DXRBS FSRQ is not anomalous. A slightly larger percentage of these objects is found among the FSRQ in the RGB survey (Laurent-Muehleisen et al. 1998, Padovani et al., in preparation), which goes to somewhat larger values of $L_{\rm x}/L_{\rm r}$ but at higher X-ray flux than DXRBS. Moreover, subsequent archival research on the *Einstein* EMSS and Slew samples (Perlman et al. 2000) has also shown similar fractions of HFSRQ.

As regards BL Lacs, DXRBS will be providing the first complete radio-selected sample down to ~ 50 mJy, an improvement of a factor of 20 in flux over the 1 Jy sample, still the only sizeable BL Lac radio-selected sample. The similar improvement in radio powers will allow us to extend the radio LF of radio-selected BL Lacs down to $L_{\rm r} \sim 10^{23-24}$ W Hz^{-1}, again getting close to the expected minimum powers according to unified schemes (Urry & Padovani 1995). Moreover, due to their low X-ray fluxes, DXRBS BL Lacs are also reaching more than an order of magnitude lower $L_{\rm x}$ than, for example, the EMSS or Slew samples.

4.3 A Multiwavelength Picture of DXRBS

A broader picture of the DXRBS sample is shown in Fig. 4, which plots the $\alpha_{\rm ro}$, $\alpha_{\rm ox}$ plane for DXRBS sources. These are the usual effective spectral indices defined between the rest-frame frequencies of 5 GHz, 5,000 Å, and 1 keV. X-ray and optical fluxes have been corrected for Galactic absorption. The effective spectral indices have been k-corrected using the appropriate radio and X-ray spectral indices, available for each source. Optical fluxes at 5,000 Å have been derived and k-corrected as described in Padovani et al. (in preparation).

The dashed lines represent, from top to bottom, the loci of $\alpha_{\rm rx} = 0.85$, typical of 1 Jy quasars with $\alpha_{\rm r} \leq 0.70$ and BL Lacs, $\alpha_{\rm rx} = 0.78$, the dividing line between HBL and LBL, and $\alpha_{\rm rx} = 0.70$, the upper boundary for EMSS BL Lacs.

A few points are worth noticing in the figure:

(i) the majority of DXRBS BL Lacs occupy a somewhat intermediate area in $\alpha_{\rm rx}$ space, in between those occupied by the 1 Jy and EMSS BL Lac samples. Such objects are also being found in other *ROSAT*-based surveys, for example RGB (Laurent-Muehleisen et al. 1998, 1999), RC (Kock et al. 1996) and HQS/RASS (Nass et al. 1996). It is now clear that the bimodal distribution observed for the 1 Jy and EMSS samples (see, e.g., Fig. 12 of Padovani & Giommi 1995) was due to selection effects and that deeper surveys are now filling the gap in parameter space. Note that due to our X-ray and radio flux limits only a handful of DXRBS BL Lacs have effective spectral indices typical of classical HBL (e.g., the EMSS sample).

(ii) DXRBS quasars have significantly lower ($P >$ 99.99%) $\alpha_{\rm rx}$ than 1 Jy quasars: $\alpha_{\rm rx} = 0.82 \pm 0.01$ versus 0.86 ± 0.01. This corresponds to an X-ray-to-radio luminosity ratio on average a factor of 2 larger for DXRBS. As discussed above, DXRBS, by reaching relatively deep radio fluxes, is sampling the low $\alpha_{\rm rx}$ (high $L_{\rm x}/L_{\rm r}$) end of the quasar distribution. In particular, 28% of DXRBS FSRQ have $\alpha_{\rm rx}$ values typical of HBL, as compared to only 3% for the 1 Jy sample.

(iii) NLRG are concentrated towards the bottom right-hand corner of the diagram and are characterized by relatively low $\alpha_{\rm ro}$ values (~ 0.4) and relatively high $\alpha_{\rm ox}$ values (~ 1.7). This is due to the strong thermal (stellar) component present in these sources. Note that although some BL Lacs are also present in this region, the mean $\alpha_{\rm ox}$ values for the two classes (1.38 ± 0.06 and 1.69 ± 0.09 for BL Lacs and radio galaxies respectively) are significantly different ($P = 99.6\%$).

(iv) still unclassified sources are, on average, fainter in all bands than identified ones but mostly so in the X-rays. This explains the fact that they occupy the high $\alpha_{\rm rx}$ part of the $\alpha_{\rm ro}$, $\alpha_{\rm ox}$ plane, the region typical of extreme FSRQ.

The impact of these findings, both for BL Lac and FSRQ, on our multiwavelength picture of the blazar class will be discussed in a future paper.

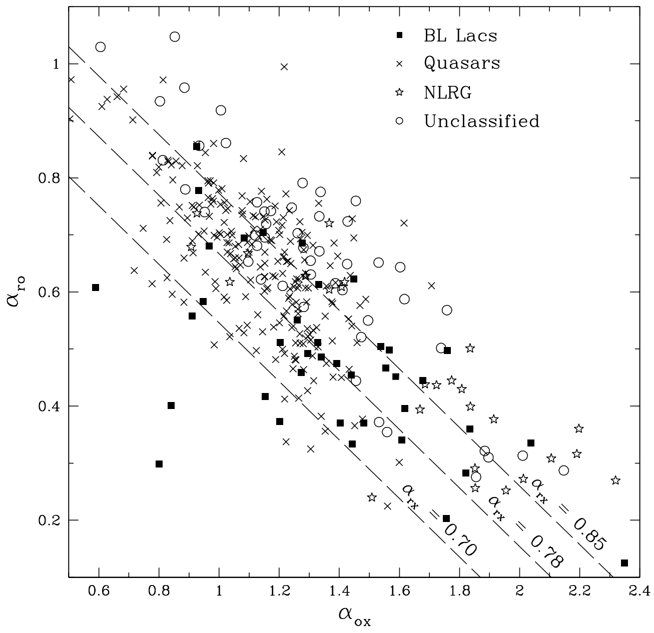

Figure 4. The $\alpha_{\rm ro}$, $\alpha_{\rm ox}$ plane for DXRBS sources. BL Lac objects are shown as filled squares, quasars as crosses, NLRG as stars, while still unidentified sources are shown as open circles. Effective spectral indices are defined the usual way and calculated between the rest-frame frequencies of 5 GHz, 5000 Å, and 1 keV. The dashed lines represent, from top to bottom, the loci of $\alpha_{\rm rx} = 0.85$, typical of 1 Jy quasars with $\alpha_{\rm r} \leq 0.70$ and BL Lacs, $\alpha_{\rm rx} = 0.78$, the dividing line between HBL and LBL, and $\alpha_{\rm rx} = 0.70$, the upper boundary for EMSS BL Lacs.

5 CONCLUSIONS

DXRBS takes advantage of three of the most dominant blazar properties, namely relatively strong X-ray and radio emission, and a flat radio spectrum, to select a large sample of flat-spectrum radio quasars and BL Lacs. Reaching 5 GHz radio fluxes ~ 50 mJy and $0.1 - 2.0$ keV X-ray fluxes a few $\times 10^{-14}$ erg cm^{-2} s^{-1}, DXRBS is the faintest and largest flat-spectrum radio sample available to date mapping previously unexplored regions of parameter space.

As of July 2000, our sample is $\sim 85\%$ identified and contains 298 sources, of which 234 (79%) are quasars, 36 (12%) are BL Lacs and 28 (9%) are radio galaxies. Thus our technique has an efficiency of $\sim 90\%$ at finding radio-loud quasars and BL Lacs. We have a measured redshift for 96% of our identified objects.

Our main results are the following:

(i) The DXRBS finds a large fraction of quasars at high redshift: 30% of DXRBS quasars have $z > 2$ (once the effect of the WGACAT sky coverage is taken into account), as compared to 15% of the quasars with $\alpha_{\rm r} \leq 0.70$ in the 1 Jy and S4 surveys combined.

(ii) The DXRBS has vastly expanded coverage of the faint end of the radio luminosity function both for BL Lacs and FSRQ. Forty of our 181 DXRBS FSRQ are at $L_{\rm r} < 10^{25.5}$ W Hz^{-1}, compared to only 10 out of 300 in the 1 Jy and S4 samples combined. Five of these are in the luminosity range $10^{24.5} < L_{\rm r} < 10^{26.5}$ W Hz^{-1}, the former being the expected minimum luminosity of FSRQ assuming these objects are beamed FR II radio galaxies.

As regards BL Lacs, DXRBS will be providing the first complete radio-selected sample down to ~ 50 mJy, an improvement of a factor of 20 in flux over the 1 Jy sample, still the only sizeable BL Lac radio-selected sample. The similar improvement in radio powers will allow us to extend the radio LF of radio-selected BL Lacs down to $L_{\rm r} \sim 10^{23-24}$ W Hz^{-1}, again getting close to the expected minimum powers according to unified schemes.

(iii) DXRBS has filled large holes in the coverage of the

$(L_{\rm x}, L_{\rm r})$ parameter space, both for quasars and BL Lacs. Prior to DXRBS, basically no FSRQ within complete samples were known at values of $L_{\rm x}/L_{\rm r} > 10^{-6}$, while 28% of FSRQ in our sample fall in this category. The discovery of such objects raises new challenges for our understanding of blazar physics.

DXRBS contains a large number of BL Lacs with $10^{-6.5} < L_{\rm x}/L_{\rm r} < 10^{-5.5}$, that is with spectral shapes "intermediate" between the "classical" radio- and X-ray selected sources. Such objects are also being found in other *ROSAT*-based surveys, which shows that the bimodal distribution observed for the 1 Jy and EMSS samples was simply due to selection effects.

The fraction of identified sources in the DXRBS sample is now large enough to allow us to study its evolutionary properties, luminosity function, and implications for unified schemes at low powers. We will address these issues in future publications.

ACKNOWLEDGEMENTS

This paper is based on observations collected at the European Southern Observatory, La Silla, Chile (proposals ESO N. 60.B-0313, 61.B-0288, and 62.P-0257), Kitt Peak National Observatory, and the Australia Telescope Compact Array, Narrabri, Australia. H.L. acknowledges financial support from the Deutscher Akademischer Austauschdienst (DAAD). P.P., E.P., and H.L. acknowledge ESO and KPNO personnel for their assistance during the observing runs. E.P. acknowledges ATNF personnel, especially John Reynolds, Robin Wark and Henrietta May, for their assistance before, during, and after ATCA observing runs. We wish to thank Dave Jauncey and Sandra Savaglio for a careful reading of the manuscript and Tommaso Treu for obtaining two of our spectra at the ESO 3.6 m telescope in August 1999. We acknowledge Isobel Hook, Peter Shaver, Meg Urry, and John Stocke for useful discussions and Isobel Hook and Anna Wolter for providing us with the identifications of some sources prior to publication. This research has made use of the BROWSE program developed by the ESA *EXOSAT* observatory and by NASA HEASARC, of the NASA/IPAC Extragalactic Database (NED), which is operated by the Jet Propulsion Laboratory, California Institute of Technology, under contract with the National Aeronautics and Space Administration, and of the STScI Digitized Sky Survey, the ROE/NRL COSMOS service, and the RGO/APM service. The Digitized Sky Surveys were produced at the Space Telescope Science Institute under U.S. Government grant NAG W-2166. The images of these surveys are based on photographic data obtained using the Oschin Schmidt Telescope on Palomar Mountain and the UK Schmidt Telescope. The plates were processed into the present compressed digital form with the permission of these institutions. The UK Schmidt Telescope was operated by the Royal Observatory Edinburgh, with funding from the UK Science and Engineering Research Council (later the UK Particle Physics and Astronomy Research Council), until 1988 June, and thereafter by the Anglo-Australian Observatory. The blue plates of the southern Sky Atlas and its Equatorial Extension (together known as the SERC-J), as well as the Equatorial Red (ER), and the Second Epoch [red] Survey (SES) were all taken with the UK Schmidt.

REFERENCES

Albrecht M. A., Brighton A., Herlin T., Biereichel P., Durand D., 1997, http://archive.eso.org/skycat
Angel J. R. P., Stockman H. S., 1980, ARA&A, 18, 321
Blandford R. D., Rees M. J., 1978, in Pittsburgh Conference on BL Lac Objects, ed. Wolfe, A. N., 328
Cao L., Wei J.-Y., Hu J.-Y., 1999, A&AS, 135, 243
Condon J. J., Cotton W. D., Greisen E. W., Yin Q. F., Perley R. A., Taylor G. B., Broderick J. J., 1998, AJ, 115, 169
Corbett E. A., Robinson A., Axon D. J., Hough J. H., Jeffries R. D., Thurston M. R., Young S., 1996, MNRAS, 281, 737
Drinkwater M. J., Barnes D. G., Ellison S. L., 1995, PASA, 13, 12
Drinkwater M. J., Webster R. L., Francis P. J., Condon J. J., Ellison S. L., Jauncey D. L., Lovell J., Peterson B. A., Savage A., 1997, MNRAS, 284, 85
Falco E. E., Kochanek C. S., Muñoz J. A., 1998, ApJ, 494, 47
Fanaroff B. L., Riley J. M., 1974, MNRAS, 167, 31
Gioia I. M., Henry J. P., Maccacaro T., Morris S. L., Stocke J. T., Wolter A., 1990, ApJ, 356, 35
Gregory P. C., Scott W. K., Douglas K., Condon J. J., 1996, ApJS, 103, 427
Griffith M. R., Wright A. E., 1993, AJ, 105, 1666
Helfand D. J., Schnee S., Becker R. H., White R. L., McMahon R. G., 1999, AJ, 117, 1568
Henstock D. R., Browne I. W. A., Wilkinson P. N., McMahon R. G., 1997, MNRAS, 290, 380
Impey C. D., Tapia S., 1990, ApJ, 354, 124
Irwin M., Maddox S., McMahon R. G., 1994, Spectrum, 2, 14
Jauncey D. L., Batty M. J., Gulkis S., Savage A., 1982, AJ, 87, 763
Kock A., Meisenheimer K., Brinkmann W., Neumann M., Siebert J., 1996, A&A, 307, 475
Kollgaard R. I., Palma C., Laurent-Muehleisen S. A., Feigelson E. D., 1996, ApJ, 465, 115
Laurent-Muehleisen S. A., Kollgaard R. I., Ciardullo R., Feigelson E. D., Brinkmann W., Siebert J., 1998, ApJS, 118, 127
Laurent-Muehleisen S. A., Kollgaard R. I., Feigelson E. D., Brinkmann W., Siebert J., 1999, ApJ, 525, 127
Loveday J., 1996, MNRAS, 278, 1025
Marchã M. J. M., Browne I. W. A., 1995, MNRAS, 275, 951
Marchã M. J. M., Browne I. W. A., Impey C. D., Smith P. S., 1996, MNRAS, 281, 425
Murphy D. W., Browne I. W. A., Perley R. A., 1993, MNRAS, 264, 298
Nass P., Bade N., Kollgaard R. I., Laurent-Muehleisen S. A., Reimers D., Voges W., 1996, A&A, 309, 419
O'Dea C. P., 1998, PASP, 110, 493
Orr M. J. L., Browne I. W. A., 1982, MNRAS, 200, 1067
Padovani P., 1997, in Very High Energy Phenomena in the Universe, ed. Y. Giraud-Héraud & J. Trân Thanh Vân (Paris: Ed. Frontieres), 7.
Padovani P., Urry C. M., 1990, 356, 75
Padovani P., Giommi P., 1995, ApJ, 444, 567
Padovani P., Giommi P., 1996, MNRAS, 279, 526
Padovani P., Giommi P., Fiore F., 1997, Mem. Soc. Astron. Italiana, 68, 147
Perlman E. S., Stocke J. T., 1993, ApJ, 406, 430

Perlman E. S., Stocke J. T., Schachter J. F., Elvis M., Ellingson E., Urry C. M., Potter M., Impey C. D., Kolchinsky P., 1996a, ApJS, 104, 251
Perlman E. S., Stocke J. T., Wang Q. D., Morris S. L., 1996b, ApJ, 456, 451
Perlman E. S., Padovani P., Giommi P., Sambruna R., Laurence R. J., Tzioumis A., Reynolds J., 1998, AJ, 115, 1253 (Paper I)
Perlman E. S., Schachter J. F., Stocke J. T., Caditz D., Rector T. A., 2000, in prep.
Rector T. A., Stocke J. T., Perlman E. S., 1999, ApJ, 516, 145
Rector T. A., Stocke J. T., Perlman E. S., Morris S. L., Gioia I. M., 2000, AJ, 120, 1626
Stark A. A., Gammie C. F., Wilson R. W., Bally J., Linke R. A., Heiles C., Hurwitz M., 1992, ApJS, 79, 77
Stickel M., Padovani P., Urry C. M., Fried J. W., Kühr H., 1991, ApJ, 374, 431
Stickel M., Kühr H., 1994, A&AS, 105, 67
Stickel M., Meisenheimer K., & Kühr H., 1994, A&AS, 105, 211
Stocke J. T., Rector T. A., 1997, ApJ, 489, L17
Urry C. M., Padovani P., 1995, PASP, 107, 803
Urry C. M., Padovani P., Stickel M., 1991, ApJ, 382, 501
Vermeulen R. C., Ogle P. M., Tran H. D., Browne I. W. A., Cohen M. H., Readhead A. C. S., Taylor G. B., Goodrich R. W., 1995, ApJS, 452, L5
White R. L., Becker R. H., 1992, ApJS, 79, 331
White N. E., Giommi P., Angelini L., 1995, http://lheawww.gsfc.nasa.gov/users/white/wgacat/wgacat.html

APPENDIX

We present here the optical spectra for the 106 DXRBS sources discussed in this paper. The wavelength in Å is plotted on the x-axis while the y-axis gives the flux f_λ in units of 10^{-17} erg cm^{-2} s^{-1} Å^{-1}.

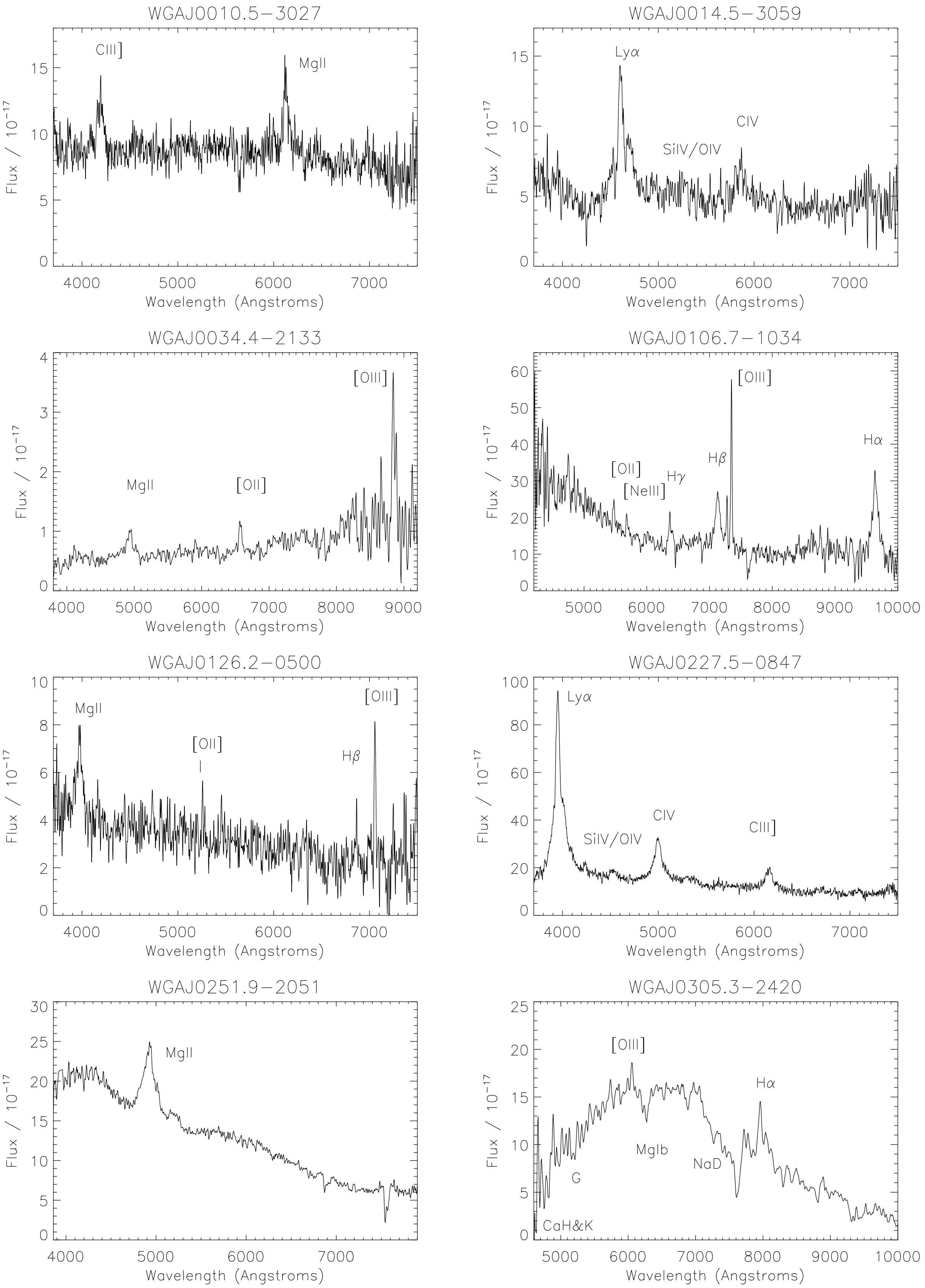
WGAJ0010.5−3027
CIII]
MgII
WGAJ0014.5−3059
Lyα
SiIV/OIV
CIV
WGAJ0034.4−2133
MgII
[OII]
[OIII]
WGAJ0106.7−1034
[OII]
[NeIII]
Hγ
Hβ
[OIII]
Hα
WGAJ0126.2−0500
MgII
[OII]
Hβ
[OIII]
WGAJ0227.5−0847
Lyα
SiIV/OIV
CIV
CIII]
WGAJ0251.9−2051
MgII
WGAJ0305.3−2420
[OIII]
Hα
MgIb
NaD
G
CaH&K
Flux / 10^{-17}
Wavelength (Angstroms)

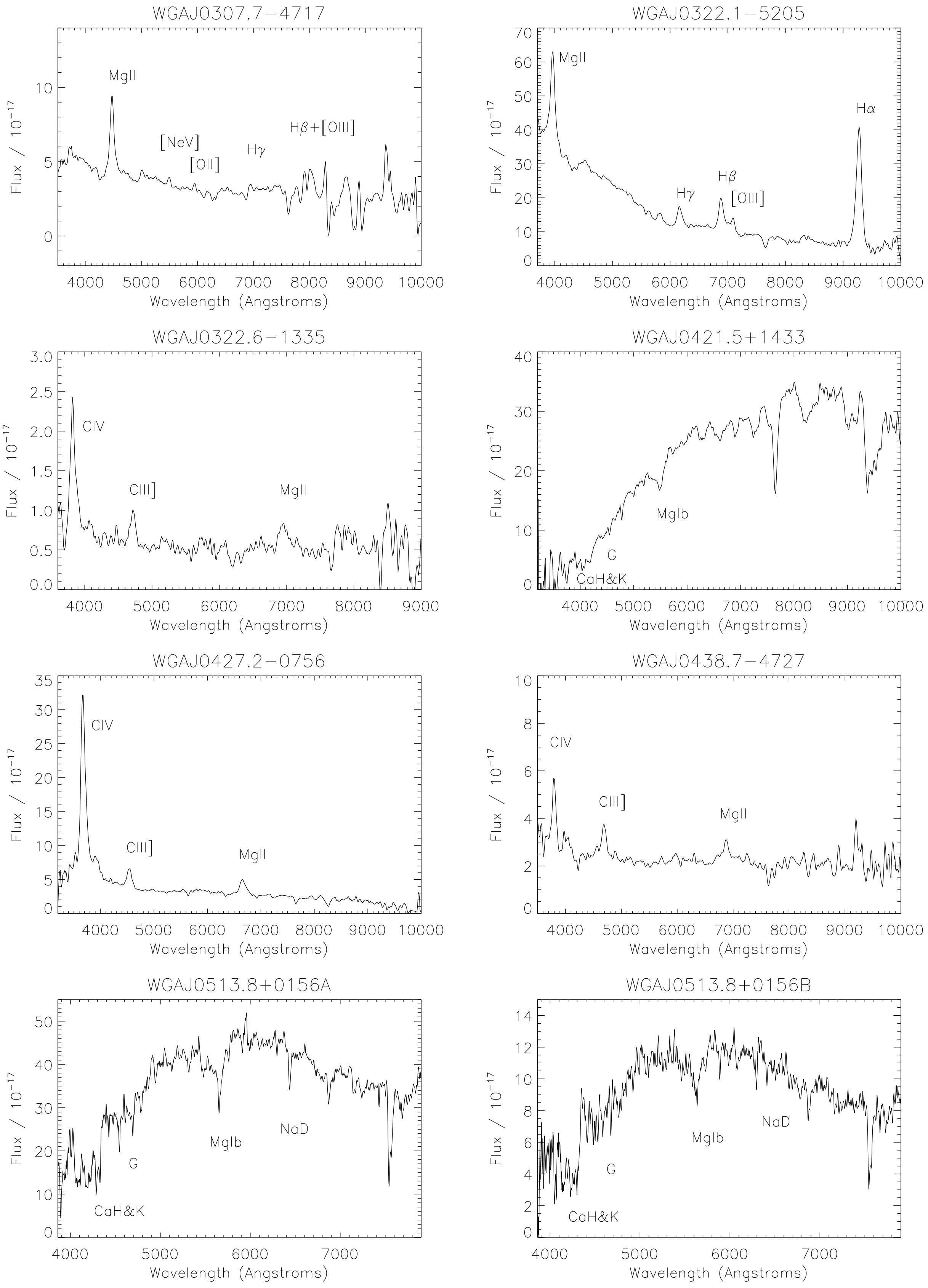
WGAJ0307.7−4717
MgII
[NeV]
[OII]
Hγ
Hβ+[OIII]
WGAJ0322.1−5205
MgII
Hα
Hγ
Hβ
[OIII]
WGAJ0322.6−1335
CIV
CIII]
MgII
WGAJ0421.5+1433
MgIb
G
CaH&K
WGAJ0427.2−0756
CIV
CIII]
MgII
WGAJ0438.7−4727
CIV
CIII]
MgII
WGAJ0513.8+0156A
MgIb
NaD
G
CaH&K
WGAJ0513.8+0156B
MgIb
NaD
G
CaH&K
Flux / 10^{-17}
Wavelength (Angstroms)

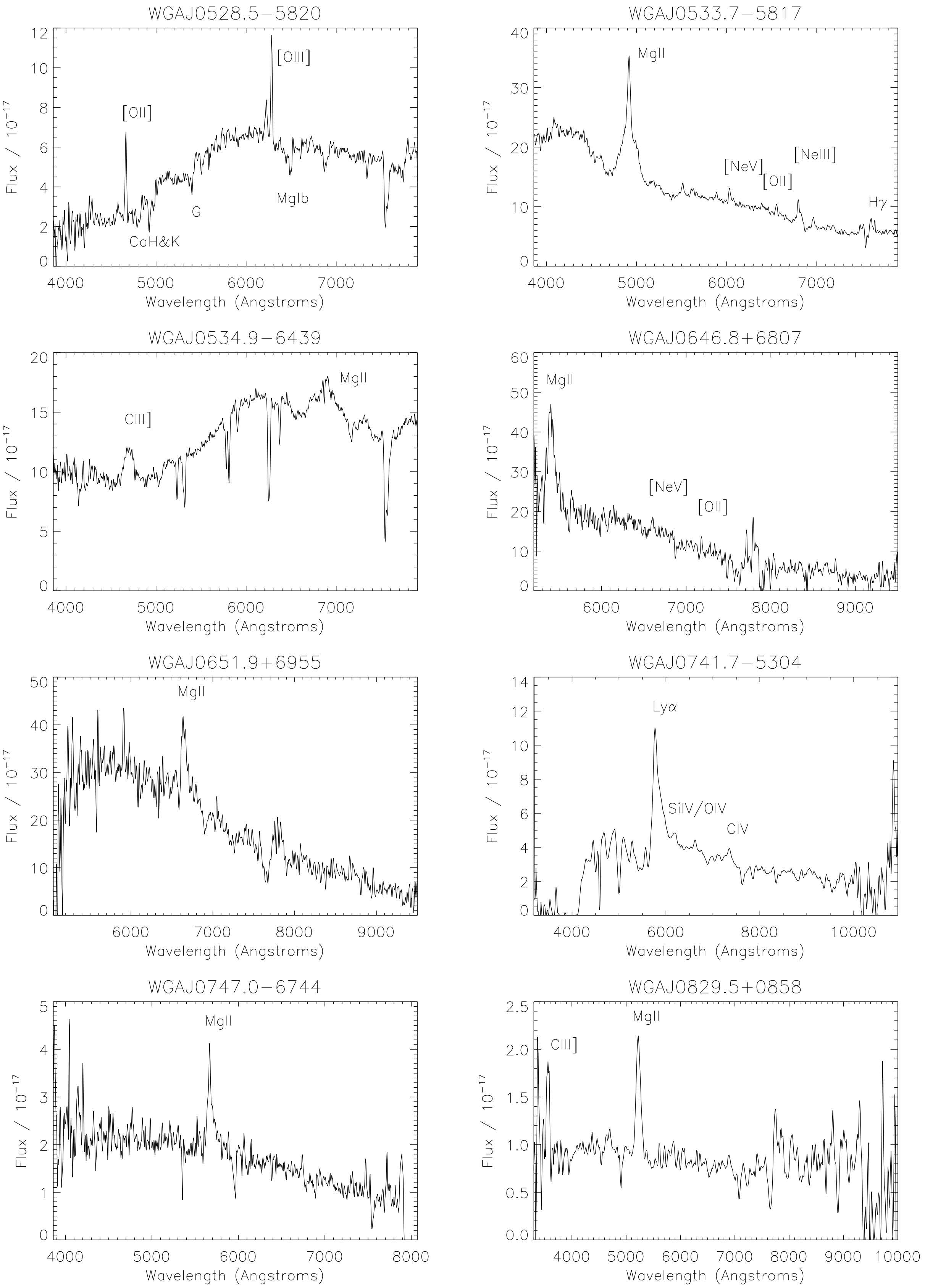
WGAJ0528.5−5820
[OII]
[OIII]
CaH&K
G
MgIb
WGAJ0533.7−5817
MgII
[NeV]
[OII]
[NeIII]
Hγ
WGAJ0534.9−6439
CIII]
MgII
WGAJ0646.8+6807
MgII
[NeV]
[OII]
WGAJ0651.9+6955
MgII
WGAJ0741.7−5304
Lyα
SiIV/OIV
CIV
WGAJ0747.0−6744
MgII
WGAJ0829.5+0858
CIII]
MgII
Flux / 10−17
Wavelength (Angstroms)

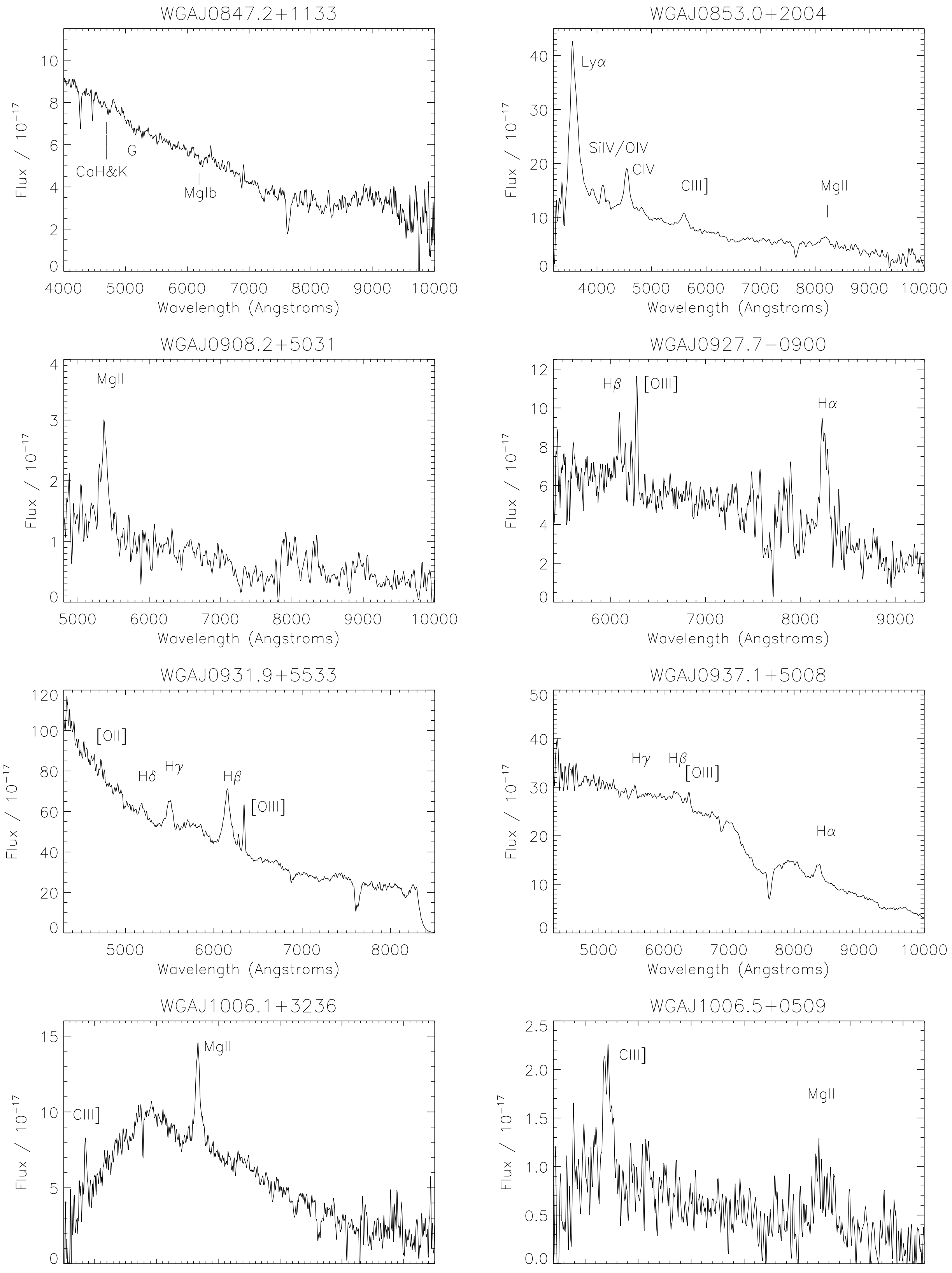
WGAJ0847.2+1133
CaH&K
G
MgIb
WGAJ0853.0+2004
Lyα
SiIV/OIV
CIV
CIII]
MgII
WGAJ0908.2+5031
MgII
WGAJ0927.7−0900
Hβ
[OIII]
Hα
WGAJ0931.9+5533
[OII]
Hδ
Hγ
Hβ
[OIII]
WGAJ0937.1+5008
Hγ
Hβ
[OIII]
Hα
WGAJ1006.1+3236
CIII]
MgII
WGAJ1006.5+0509
CIII]
MgII
Flux / 10^{-17}
Wavelength (Angstroms)

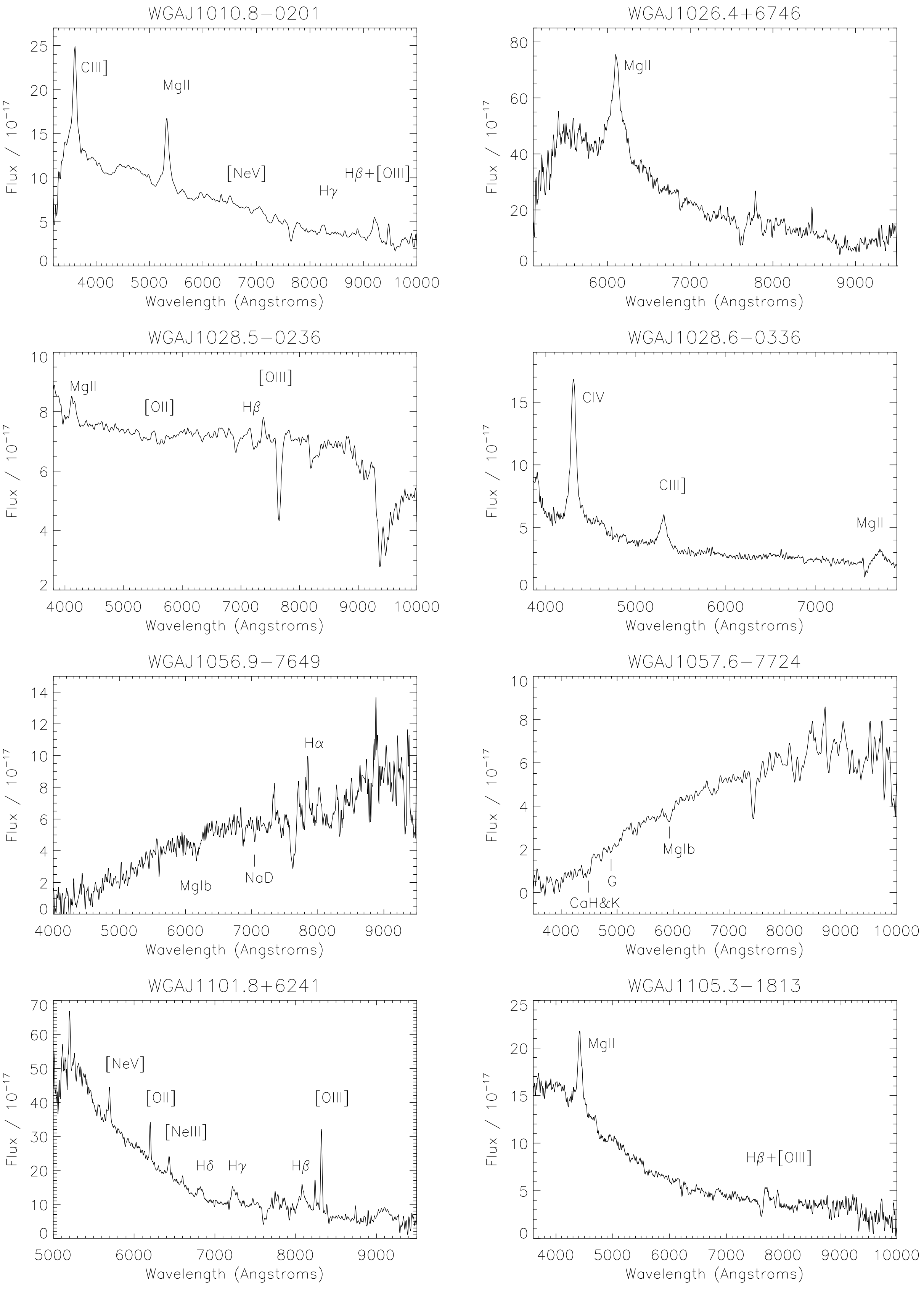
WGAJ1010.8−0201
CIII]
MgII
[NeV]
Hγ
Hβ+[OIII]
Flux / 10^−17
Wavelength (Angstroms)
WGAJ1026.4+6746
MgII
Flux / 10^−17
Wavelength (Angstroms)
WGAJ1028.5−0236
MgII
[OII]
Hβ
[OIII]
Flux / 10^−17
Wavelength (Angstroms)
WGAJ1028.6−0336
CIV
CIII]
MgII
Flux / 10^−17
Wavelength (Angstroms)
WGAJ1056.9−7649
Hα
MgIb
NaD
Flux / 10^−17
Wavelength (Angstroms)
WGAJ1057.6−7724
MgIb
G
CaH&K
Flux / 10^−17
Wavelength (Angstroms)
WGAJ1101.8+6241
[NeV]
[OII]
[NeIII]
Hδ
Hγ
Hβ
[OIII]
Flux / 10^−17
Wavelength (Angstroms)
WGAJ1105.3−1813
MgII
Hβ+[OIII]
Flux / 10^−17
Wavelength (Angstroms)

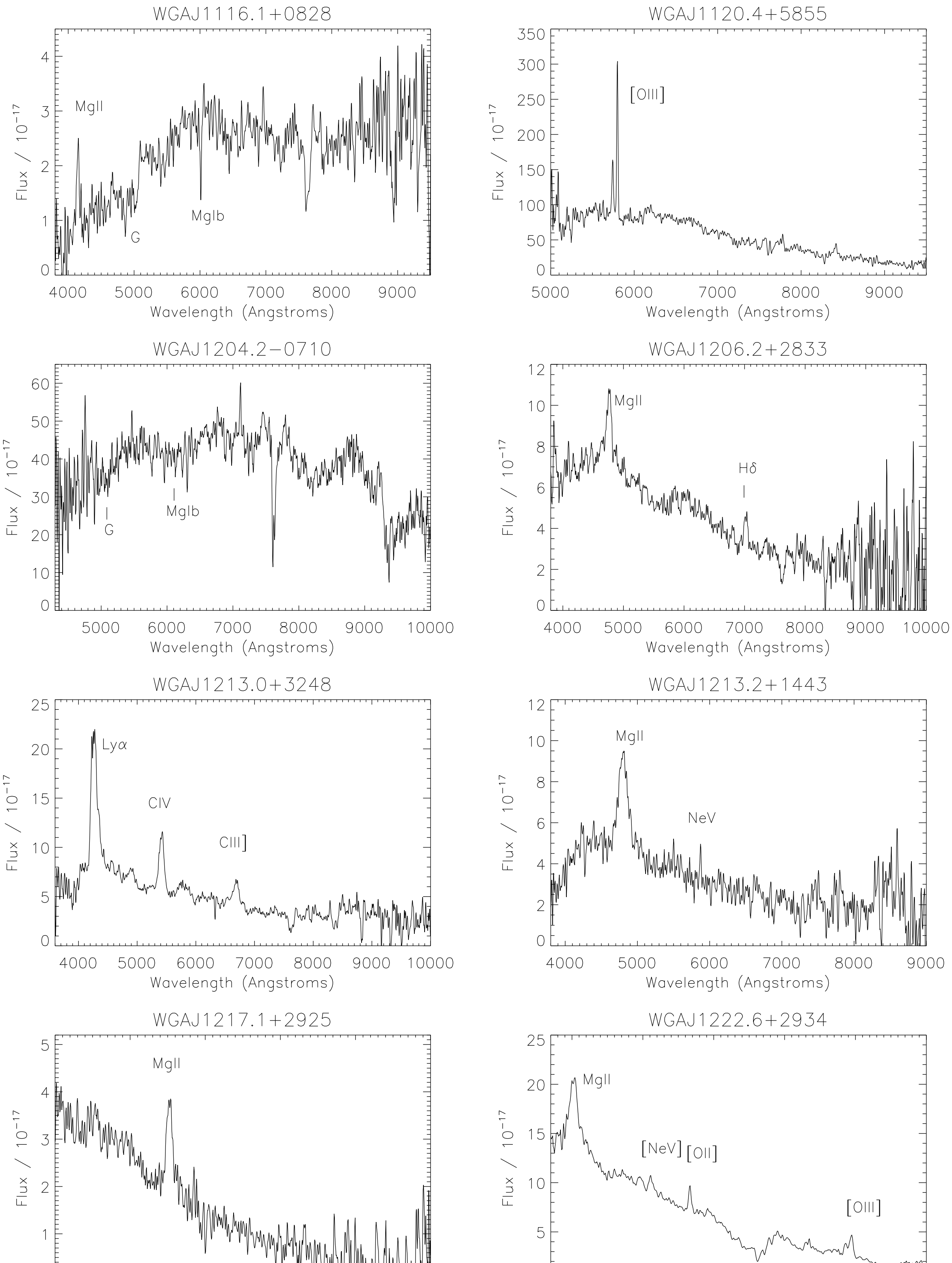

WGAJ1116.1+0828
MgII
G
MgIb
WGAJ1120.4+5855
[OIII]
WGAJ1204.2−0710
G
MgIb
WGAJ1206.2+2833
MgII
Hδ
WGAJ1213.0+3248
Lyα
CIV
CIII]
WGAJ1213.2+1443
MgII
NeV
WGAJ1217.1+2925
MgII
WGAJ1222.6+2934
MgII
[NeV]
[OII]
[OIII]
Flux / 10^−17
Wavelength (Angstroms)

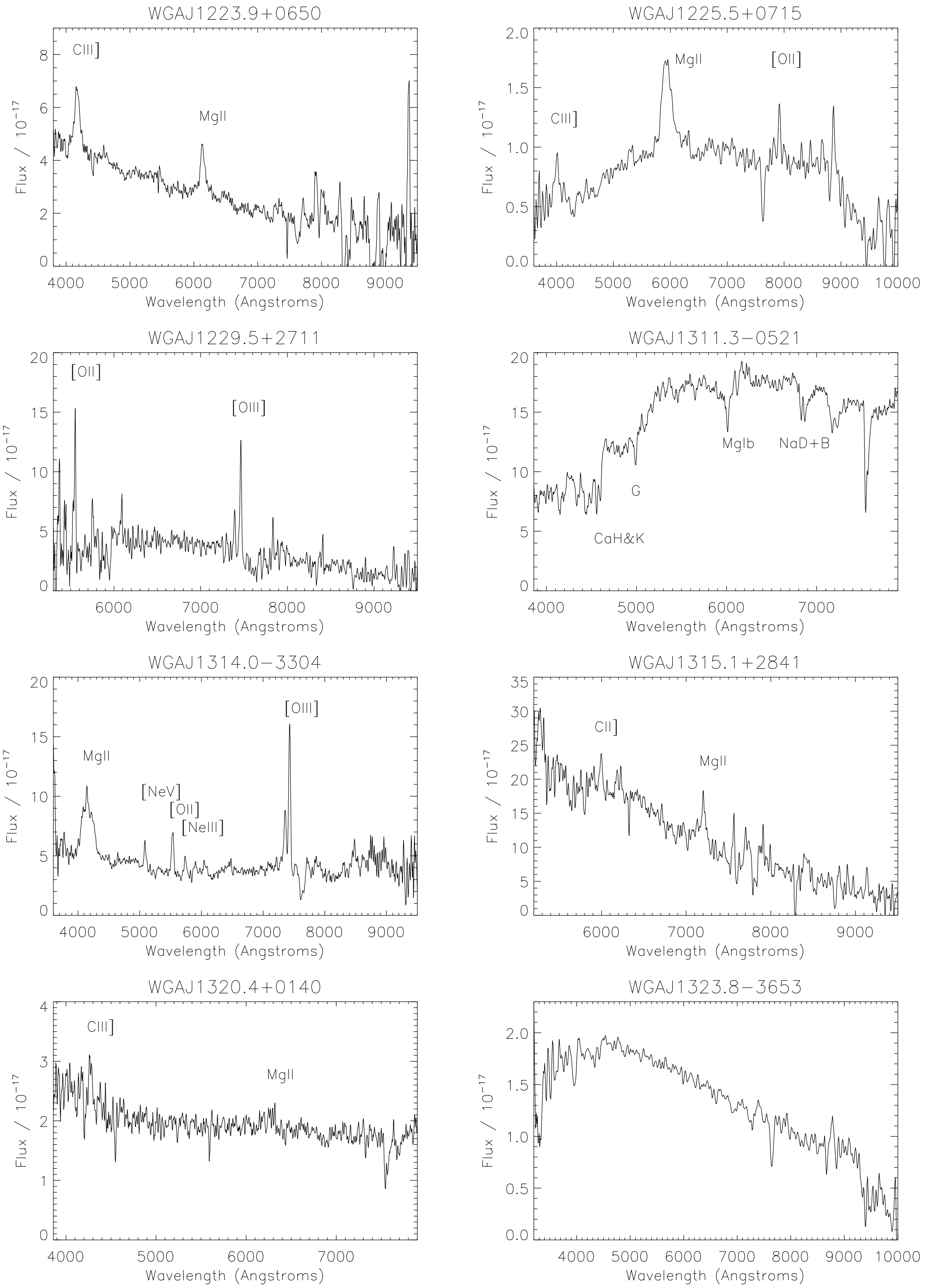
WGAJ1223.9+0650
CIII]
MgII
WGAJ1225.5+0715
MgII
[OII]
CIII]
WGAJ1229.5+2711
[OII]
[OIII]
WGAJ1311.3−0521
MgIb
NaD+B
G
CaH&K
WGAJ1314.0−3304
[OIII]
MgII
[NeV]
[OII]
[NeIII]
WGAJ1315.1+2841
CII]
MgII
WGAJ1320.4+0140
CIII]
MgII
WGAJ1323.8−3653
Flux / 10^{-17}
Wavelength (Angstroms)

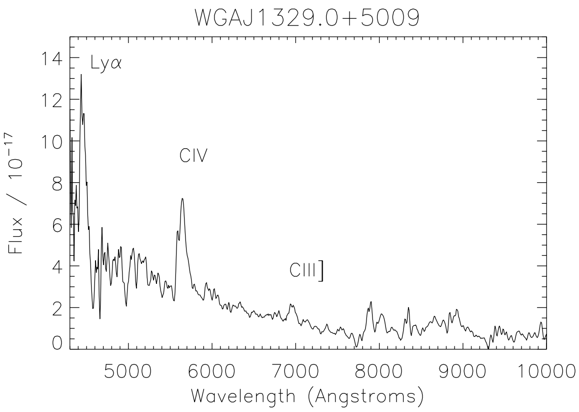
WGAJ1329.0+5009
Lyα
CIV
CIII]
Flux / 10⁻¹⁷
Wavelength (Angstroms)

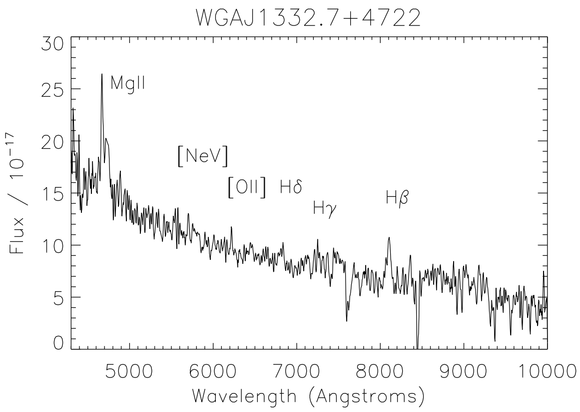
WGAJ1332.7+4722
MgII
[NeV]
[OII]
Hδ
Hγ
Hβ
Flux / 10⁻¹⁷
Wavelength (Angstroms)

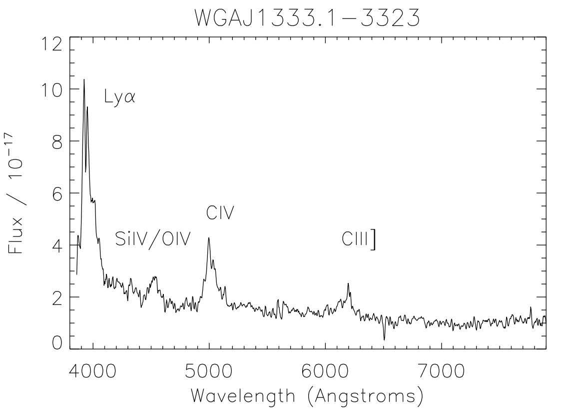
WGAJ1333.1−3323
Lyα
SiIV/OIV
CIV
CIII]
Flux / 10⁻¹⁷
Wavelength (Angstroms)

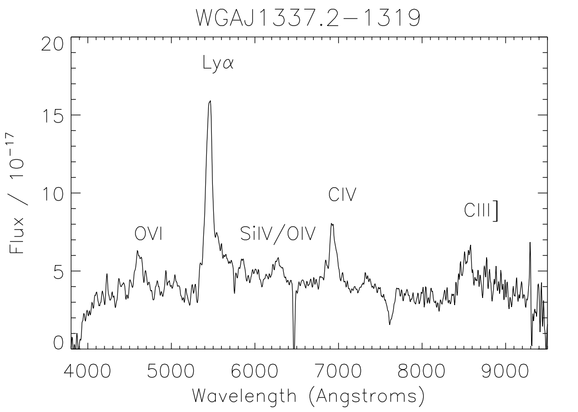
WGAJ1337.2−1319
Lyα
OVI
SiIV/OIV
CIV
CIII]
Flux / 10⁻¹⁷
Wavelength (Angstroms)

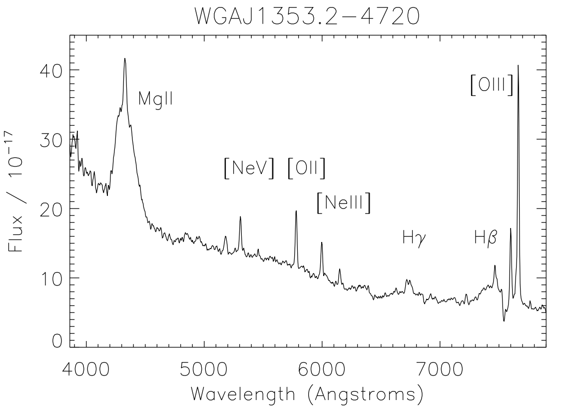
WGAJ1353.2−4720
MgII
[NeV]
[OII]
[NeIII]
Hγ
Hβ
[OIII]
Flux / 10⁻¹⁷
Wavelength (Angstroms)

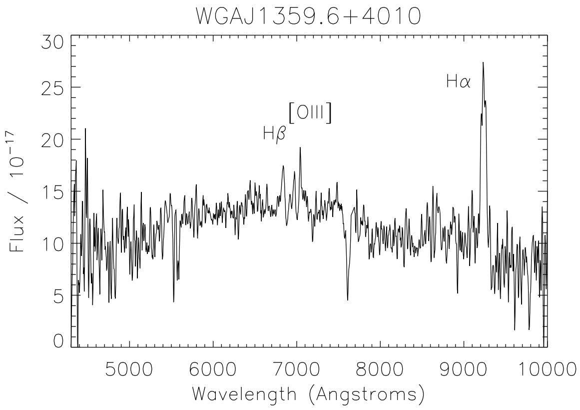
WGAJ1359.6+4010
Hβ
[OIII]
Hα
Flux / 10⁻¹⁷
Wavelength (Angstroms)

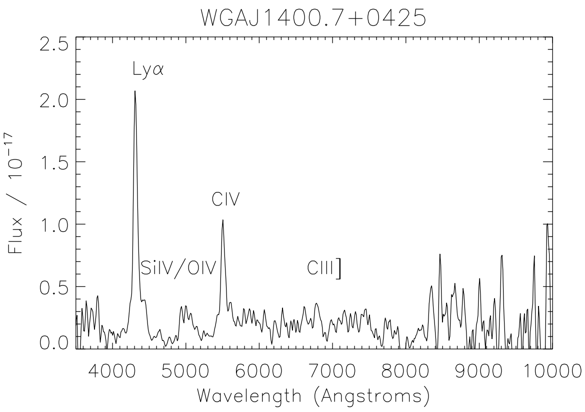
WGAJ1400.7+0425
Lyα
SiIV/OIV
CIV
CIII]
Flux / 10⁻¹⁷
Wavelength (Angstroms)

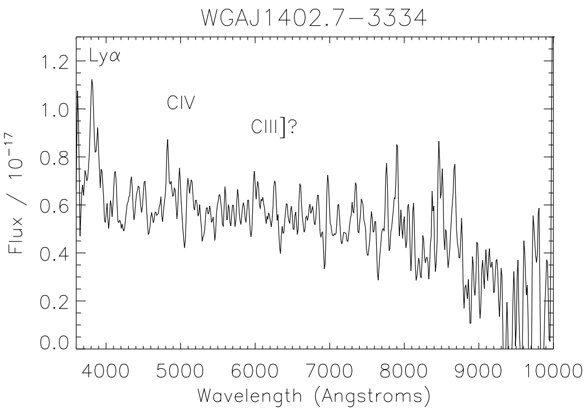
WGAJ1402.7−3334
Lyα
CIV
CIII]?
Flux / 10⁻¹⁷
Wavelength (Angstroms)

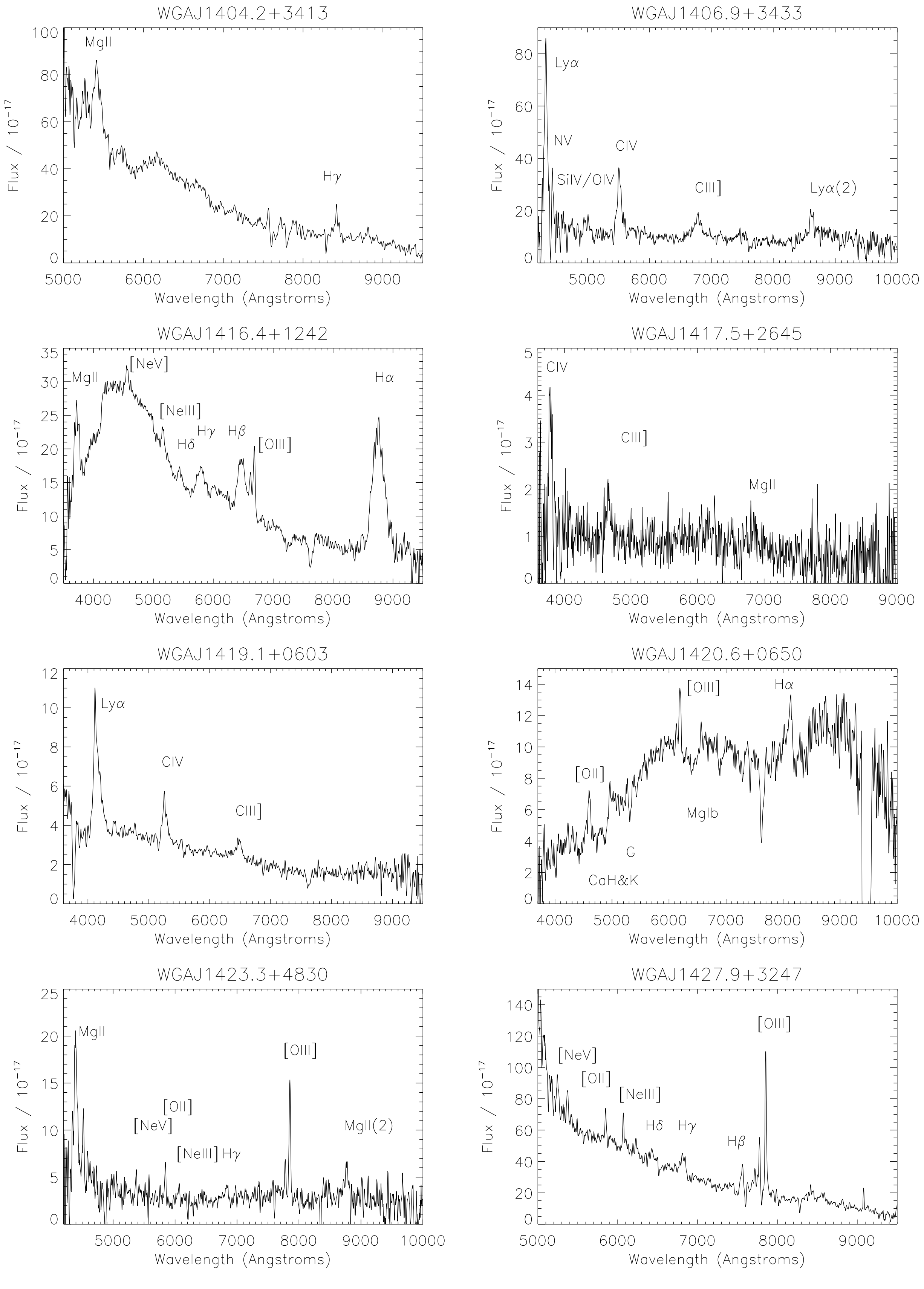
WGAJ1404.2+3413
MgII
Hγ
WGAJ1406.9+3433
Lyα
NV
SiIV/OIV
CIV
CIII]
Lyα(2)
WGAJ1416.4+1242
MgII
[NeV]
[NeIII]
Hδ
Hγ
Hβ
[OIII]
Hα
WGAJ1417.5+2645
CIV
CIII]
MgII
WGAJ1419.1+0603
Lyα
CIV
CIII]
WGAJ1420.6+0650
[OIII]
Hα
[OII]
MgIb
G
CaH&K
WGAJ1423.3+4830
MgII
[OIII]
[OII]
[NeV]
[NeIII] Hγ
MgII(2)
WGAJ1427.9+3247
[OIII]
[NeV]
[OII]
[NeIII]
Hδ
Hγ
Hβ
Flux / 10^-17
Wavelength (Angstroms)

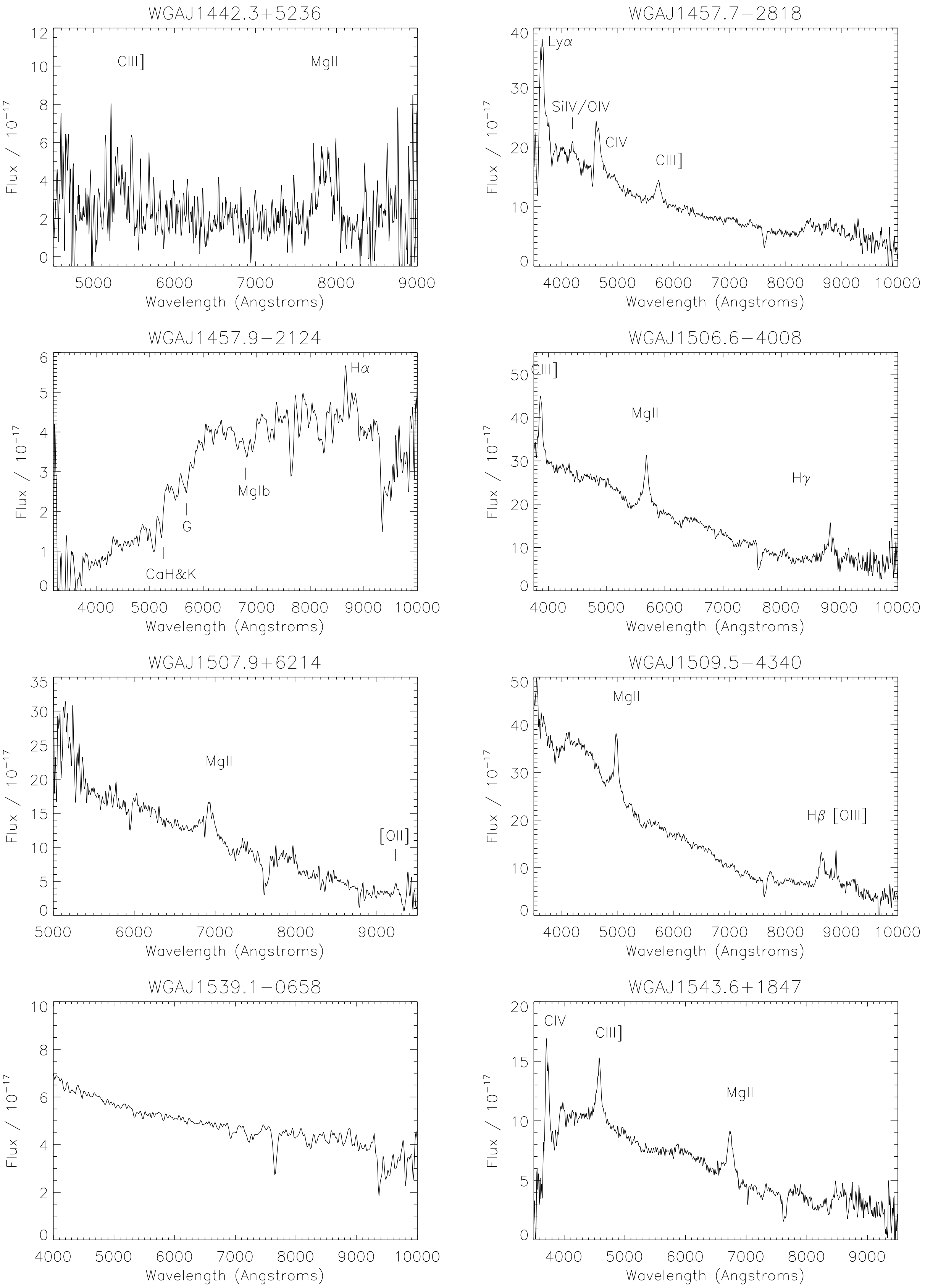
WGAJ1442.3+5236
CIII]
MgII
WGAJ1457.7−2818
Lyα
SiIV/OIV
CIV
CIII]
WGAJ1457.9−2124
Hα
MgIb
G
CaH&K
WGAJ1506.6−4008
CIII]
MgII
Hγ
WGAJ1507.9+6214
MgII
[OII]
WGAJ1509.5−4340
MgII
Hβ [OIII]
WGAJ1539.1−0658
WGAJ1543.6+1847
CIV
CIII]
MgII
Flux / 10^−17
Wavelength (Angstroms)

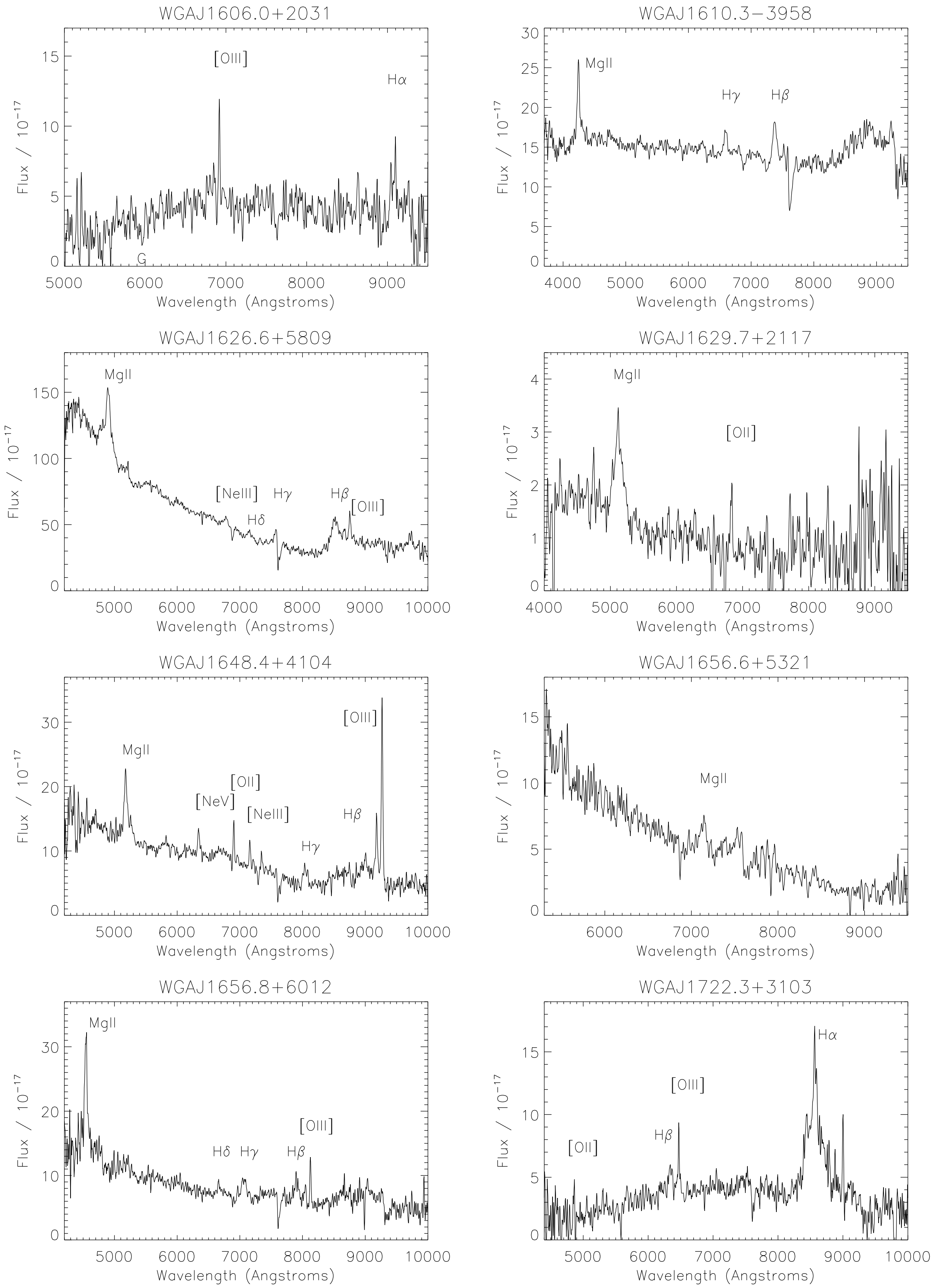
WGAJ1606.0+2031
[OIII]
Hα
G
WGAJ1610.3−3958
MgII
Hγ
Hβ
WGAJ1626.6+5809
MgII
[NeIII]
Hγ
Hβ
Hδ
[OIII]
WGAJ1629.7+2117
MgII
[OII]
WGAJ1648.4+4104
[OIII]
MgII
[OII]
[NeV]
[NeIII]
Hβ
Hγ
WGAJ1656.6+5321
MgII
WGAJ1656.8+6012
MgII
[OIII]
Hδ
Hγ
Hβ
WGAJ1722.3+3103
Hα
[OIII]
[OII]
Hβ
Flux / 10^{-17}
Wavelength (Angstroms)

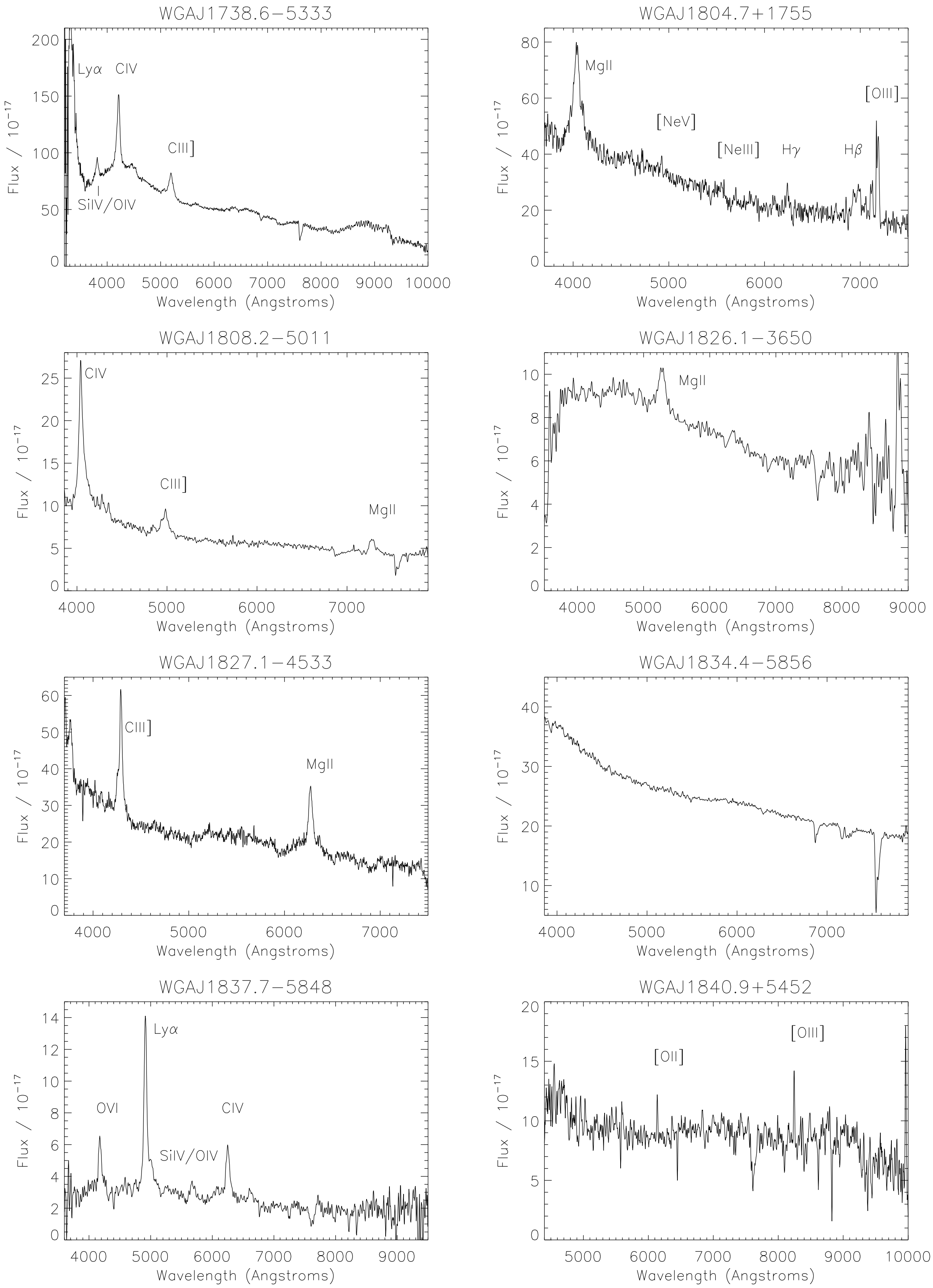

WGAJ1738.6−5333
Lyα
CIV
CIII]
SiIV/OIV
WGAJ1804.7+1755
MgII
[NeV]
[NeIII]
Hγ
Hβ
[OIII]
WGAJ1808.2−5011
CIV
CIII]
MgII
WGAJ1826.1−3650
MgII
WGAJ1827.1−4533
CIII]
MgII
WGAJ1834.4−5856
WGAJ1837.7−5848
Lyα
OVI
SiIV/OIV
CIV
WGAJ1840.9+5452
[OII]
[OIII]
Flux / 10^{-17}
Wavelength (Angstroms)

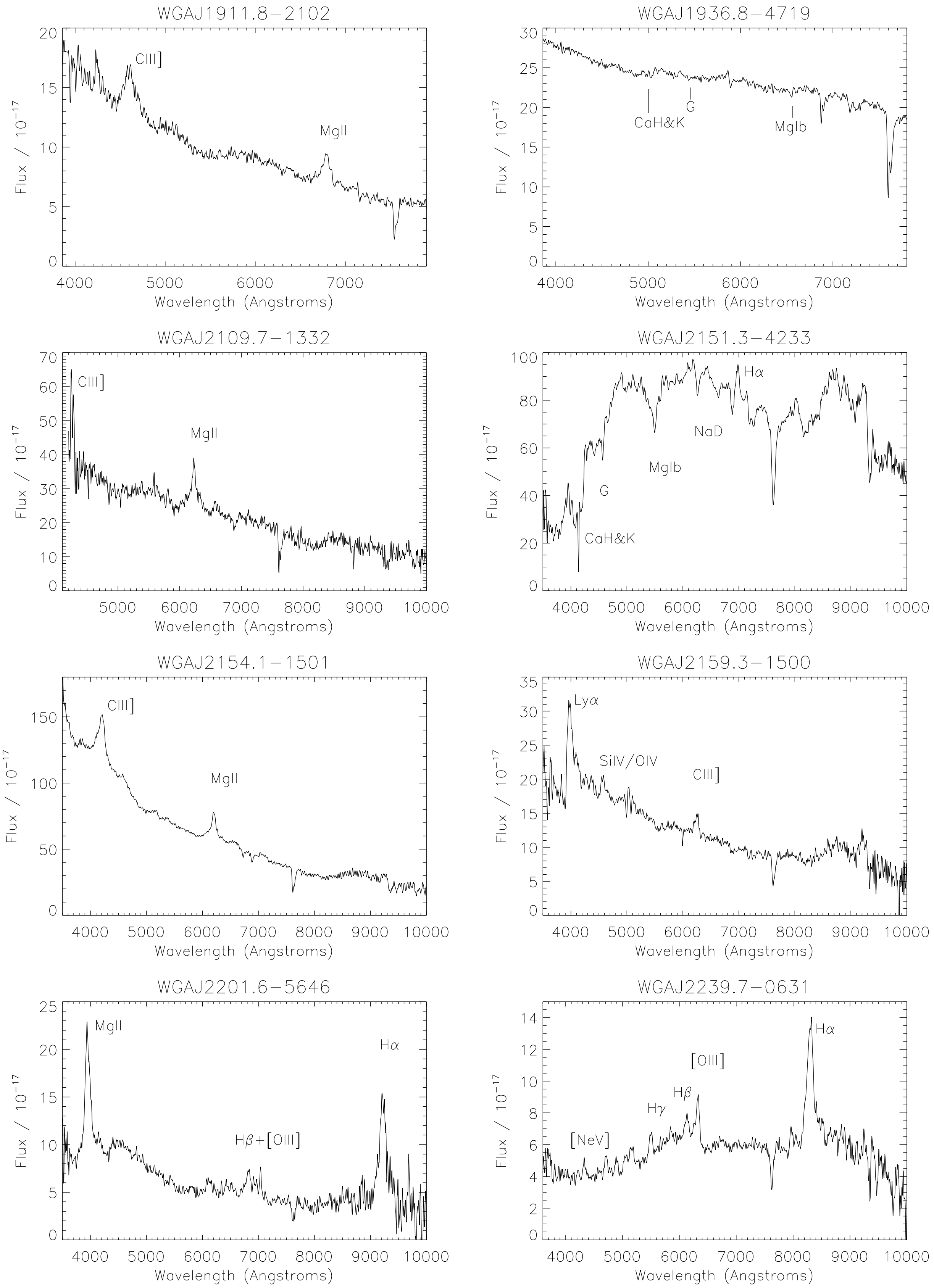
WGAJ1911.8−2102
CIII]
MgII
WGAJ1936.8−4719
CaH&K
G
MgIb
WGAJ2109.7−1332
CIII]
MgII
WGAJ2151.3−4233
Hα
NaD
MgIb
G
CaH&K
WGAJ2154.1−1501
CIII]
MgII
WGAJ2159.3−1500
Lyα
SiIV/OIV
CIII]
WGAJ2201.6−5646
MgII
Hα
Hβ+[OIII]
WGAJ2239.7−0631
Hα
[OIII]
Hβ
Hγ
[NeV]
Flux / 10^{-17}
Wavelength (Angstroms)

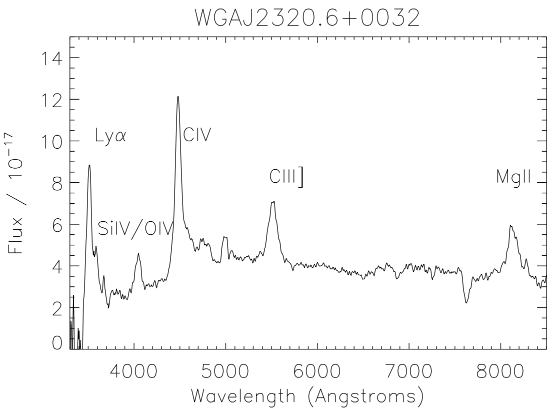

WGAJ2320.6+0032
Lyα
SiIV/OIV
CIV
CIII]
MgII
Flux / 10^-17
Wavelength (Angstroms)

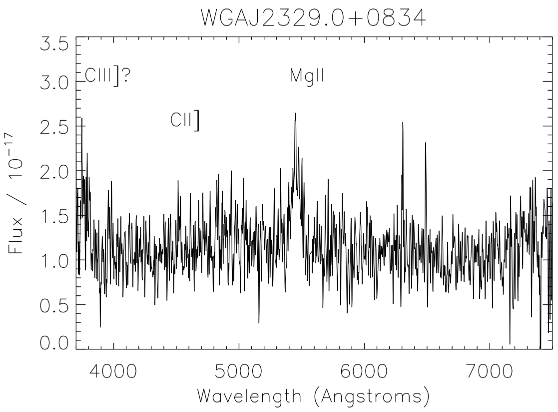

WGAJ2329.0+0834
CIII]?
CII]
MgII
Flux / 10^-17
Wavelength (Angstroms)

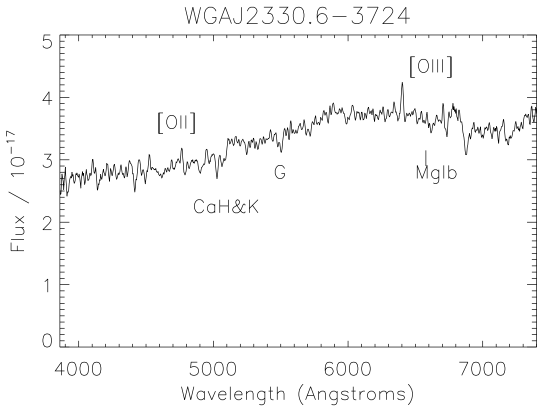

WGAJ2330.6−3724
[OII]
[OIII]
CaH&K
G
MgIb
Flux / 10^-17
Wavelength (Angstroms)